Experimental study of the effects of solute transport on reaction paths during incipient serpentinization

S. Escario *, M. Godard, P. Gouze, R. Leprovost

Géosciences Montpellier, CNRS, Univ. Montpellier, 34095 Montpellier, France
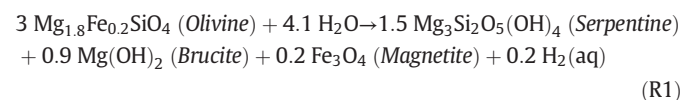
ABSTRACT

This paper presents the results of 4 reactive percolation experiments set up for investigating the impact of flow rate on serpentinization reaction paths for conditions relevant of the oceanic peridotite sub-seafloor during the initial stages of its hydrothermal alteration. The experiments consisted in injecting artificial seawater into porous compressed olivine powder cores at constant flow rates Q: 0.24, 0.48, 1.14 and 5.21 mL·h^{-1}. The experiments were conducted at constant temperature (170 °C) and pressure (25 MPa) and lasted 11 to 28 days. At the end of the experiments, the outlet fluids compositions displayed similar compositions, buffered by the formation of serpentine (aMg^{2+}/a(H^{+})^{2} = 9.7–10; aSiO$_2$ = −3.9 to −5.2; pH $_{in\ situ}$ = 6.1). These values were achieved in a few to up to 300 h for the high flow rate experiment suggesting that they corresponded to a steady-state regime of mass transfer which depended on flow rate. Differences in the composition of fluid versus time and in the structure of reacted samples during and after the four reactive percolation experiments suggested also various incipient serpentinization reaction paths. The low Q experiments produced SiO$_2$(aq) enriched outlet fluids and nodular aggregates were identified covering the reacted olivine surfaces. During high Q experiments, fibrous filaments of proto-serpentine were formed on the olivine surfaces and the fluids progressively achieved steady state compositions similar to the other experiments. These results together with those of previously published reactive percolation experiments lead us to propose two end-member reaction paths for incipient serpentinization of olivine-dominated permeable rocks infiltrated by seawater derived hydrothermal fluids: (1) a transport-controlled reaction path occurring in diffusion dominated zones is characterized by transient brucite precipitation, which produces Mg trapping and Si release in solution, followed by serpentine precipitation and (2) a kinetics-controlled reaction path occurring in advection dominated zones where transport conditions are favorable to Mg leaching and where serpentine precipitates first. The occurrence of these two end-member reaction paths is determined locally by the composition of the fluid, which varies along flow paths. Thus, both reaction paths can coexist in the sample depending on the local pore geometry. Our study shows that the interplay between fluid transport and reaction kinetics controls the chemical fluxes between the mineral surface and the bulk solution, and the incipient serpentinization reaction paths. In natural systems, the scale and distribution of these reaction domains will depend on the complex structure of the ultramafic basement. Our results suggest that the precipitation of serpentine and silica rich phases will be favored in fluid focusing zones such as faults and fractures, whilst formation of brucite will preferentially occur as part of pervasive background serpentinization.

1. Introduction

Serpentinization is ubiquitous where mantle peridotites are exposed at mid-ocean ridges along magma-starved segments and tectonic windows (e.g., reviews of Mével (2003) and Evans et al. (2013)). It is a low temperature (<350 °C) hydrothermal process resulting in the formation of hydrous minerals (serpentine, brucite, …) after olivine, a Mg-Fe-rich mineral that composes >70% of the shallow oceanic mantle (other phases being pyroxenes and minor spinel) (Bodinier and Godard (2003). Reaction for the serpentinization of the oceanic mantle is often summed up as follows:

$$3\ Mg_{1.8}Fe_{0.2}SiO_4\ (Olivine) + 4.1\ H_2O \rightarrow 1.5\ Mg_3Si_2O_5(OH)_4\ (Serpentine) + 0.9\ Mg(OH)_2\ (Brucite) + 0.2\ Fe_3O_4\ (Magnetite) + 0.2\ H_2(aq)$$

(R1)

Oceanic serpentinization is associated to redox reactions and hydrogen production (e.g. Bach et al., 2006; Evans, 2008; Oufi et al., 2002) as

* Corresponding author.
  E-mail address: Sofia.Escario@gm.univ-montp2.fr (S. Escario).

well as to carbonate formation and carbon reduction reactions when CO_2 is present (e.g., Früh-Green et al., 2004). This suite of reactions can modify the rheological (e.g., Escartín et al., 2001), geophysical (e.g., Maffione et al., 2014) and chemical (e.g., Paulick et al., 2006) properties of the oceanic mantle lithosphere. It is also an important vector of energy and chemical exchanges between the ocean and the deep lithosphere at ridges through the development of mantle hosted hydrothermal vents characterized by their unique fluid chemistry rich in H_2, CH_4 and abiotic hydrocarbons (e.g., Charlou et al., 2013).

Thermodynamic studies show that mantle minerals, olivine and pyroxene, are unstable below 450 °C and 5 kbar, and therefore highly reactive when water is present (e.g., Klein and Garrido, 2011; O'Hanley, 1996; Palandri and Reed, 2004). They indicate also that the olivine hydration reaction is exothermic (MacDonald and Fyfe, 1985) and some authors suggested that it might drive hydrothermal circulation in the oceanic ultramafic basements (e.g., Lowell and Rona, 2002). Nevertheless, the predicted range of pressures and temperatures over which serpentinization can occur is too large to accurately constrain models of hydrothermal alteration of the cooling mantle lithosphere, as it covers the full range over which these processes can take place. For these reasons, since the pioneering works of Martin and Fyfe (1970), numerous experimental studies have been devoted to understanding and constraining the chemical mechanisms driving olivine hydration and serpentinization in oceanic environments.

Experimental studies on serpentinization have been realized mostly using batch approaches with the aim of achieving equilibrium and fluid-rock reaction completion: autoclave reactors (e.g., Malvoisin et al., 2012; Marcaillou et al., 2011; Ogasawara et al., 2013; Okamoto et al., 2011) and hydrothermal gold cells (e.g., Allen and Seyfried, 2003; Berndt et al., 1996; Janecky and Seyfried, 1986; Klein and McCollom, 2013; McCollom et al., 2016; Seyfried et al., 2007; Seyfried and Dibble, 1980) at water/rock mass ratio larger than one, synthetic fluid inclusions used as micro-reactor (Lamadrid et al., 2017) and diamond-anvil cells (e.g., Andreani et al., 2013; Pens et al., 2016). In order to achieve the maximum degree of reaction over time scales consistent with laboratory studies, these experimental studies were often realized using fine grained mineral powders and/or with pure water, which provide the maximum reactive surface areas versus mineral volume ratios (e.g., Malvoisin et al., 2012; Martin and Fyfe, 1970) and the highest H_2O activity (e.g., Lamadrid et al., 2017). These experiments have demonstrated the first order dependence of the kinetics of serpentinization and associated reactions on temperature: serpentinization efficiency is the highest between 250 °C and 310 °C (e.g., Martin and Fyfe, 1970; Wegner and Ernst, 1983) whilst carbonate formation after olivine is the fastest at 185 °C (e.g., Gerdemann et al., 2007; O'Connor et al., 2001; O'Connor et al., 2005). They also pointed to the need to take into account the structural and compositional heterogeneities of the mantle basement and variations of fluid chemistry to model natural systems (e.g., Malvoisin and Brunet, 2014; Janecky and Seyfried, 1986).

The composition of the hydrothermal fluids flowing into the mantle basement at mid-oceanic ridges is expected to have highly variable compositions revealing their different sources from alkaline Mg-rich seawater derived fluids to more acidic Al- and Si-rich fluids produced by interactions with pyroxene-bearing peridotite and neighbouring basalts or gabbros (e.g., Douville et al., 2002; Seyfried et al., 2013). Laboratory experiments and thermodynamic computations show that the composition of these fluids will strongly affect serpentinization kinetics and reaction paths (e.g., Allen and Seyfried, 2003; Janecky and Seyfried, 1986; Klein et al., 2013; McCollom and Bach, 2009). Serpentinization is much faster in high pH alkaline conditions (Lafay et al., 2012; Pens et al., 2016) than experiments run under neutral conditions (e.g., Malvoisin et al., 2012; Martin and Fyfe, 1970; Ogasawara et al., 2013; Okamoto et al., 2011; Seyfried et al., 2007) although rates of olivine dissolution decrease with increasing pH (Chen and Brantley, 2000; Giammar et al., 2005; Hänchen et al., 2006; Pokrovsky and Schott, 2000a; Prigiobbe et al., 2009; Rosso and Rimstidt, 2000;

Rimstidt et al., 2012). Also olivine serpentinization kinetics is enhanced in presence of alkaline Al-rich fluids (Andreani et al., 2013; Pens et al., 2016). Furthermore, high Mg and/or Si activities in fluids determine serpentinization reaction paths by favoring or hindering the precipitation of brucite (Janecky and Seyfried, 1986; Ogasawara et al., 2013; Syverson et al., 2017; Tutolo et al., 2018) or silica-rich hydrous minerals such as talc (e.g., Evans, 2004) rather than serpentine precipitation. The development of such various intermediate reactions and secondary mineral assemblages can in turn modify the micro-scale structure of serpentinizing ultramafic basement and therefore the accessibility of the fluid to the mineral interfaces, which is a critical parameter for chemical reactions to occur.

Peridotites have low permeability (e.g., 10^{-21}–10^{-17} m^2 (Hatakeyama et al., 2017, Hirose and Hayman, 2008)) whilst serpentinization tends to clog efficiently flow paths by producing low density minerals (e.g., hydrous minerals and carbonates) at the expense of high density olivine. Nevertheless, the extensive hydrothermal alteration of the mantle lithosphere indicates that efficient mechanisms favor fluid flow into the serpentinizing mantle basement at mid-ocean ridges (e.g., Rouméjon et al., 2015; Schroeder et al., 2002). Flow paths into the mantle lithosphere probably combine localized flow along high permeability km-scale fractured zones (e.g., Farough et al., 2016; Hirose and Hayman, 2008) and pervasive fluid influx into serpentinizing rocks (e.g., Emmanuel and Berkowitz, 2006), which permeability is assumed to be maintained by the continuous formation of cracks down to the mineral scale through tectonic, thermal or/and reaction-induced stresses (e.g., Boudier et al., 2005; Kelemen and Hirth, 2012; Rouméjon et al., 2015; Rudge et al., 2010). Flow paths into the mantle lithosphere are thus governed by multi-scale heterogeneities in the rock structure (porosity, connectivity, tortuosity), and this implies that solute transport to and from reactive mineral surfaces and its effects on fluid-rock reaction pathways and kinetics will depend on these structural heterogeneities. Two complementary experimental approaches have been developed to study the interplay between chemical reactions and solute transport in peridotites during serpentinization and associated reactions. The first approach was designed to investigate the effect of diffuse transport (no fluid flow): it consisted in long duration (up to 300 days) batch experiments during which low porosity peridotites (Klein et al., 2015) and sintered olivine analogues (Malvoisin and Brunet, 2014) were reacted with water at optimal temperature and pressure for serpentinization. Serpentine and brucite were produced as predicted by thermodynamic models but, in both cases, the serpentinization kinetics were lower than reported for powder experiments (~0.01%/day compared to ~1–2%/day e.g., Marcaillou et al. (2011) on peridotite powder of 1 μm grain size) as a result of the limited olivine surface area accessible to water in porous samples. The second approach aimed at investigating the coupling and feedback effects between flow, transport and mineralogical reactions as fluids were injected into porous (Luhmann et al., 2017) and fractured (Farough et al., 2016) peridotites and in sintered olivine-rich analogues (Andreani et al., 2009; Godard et al., 2013; Peuble et al., 2015a, 2015b). Reactive percolation experiments were run over shorter durations compared to the first approach (maximum 36 days). They showed the strong effect of pore geometry and fluid flow variability triggering the development of local chemical heterogeneities, named chemical micro-environments by Steefel and Maher (2009). The flow heterogeneity which corresponds to several orders of magnitude in the local flow velocity have been identified as a critical parameter that control the nature and the efficiency of hydration processes (Godard et al., 2013) and of carbonate formation (Andreani et al., 2009; Peuble et al., 2015a, 2015b). These studies gave a first insight into the complex coupling between flow, solute transport and kinetics of dissolution and precipitation reactions at the scale of samples of few cubic centimeters (e.g. Godard et al., 2013; Luhmann et al., 2017).

Following this experimental approach, we present in this article the results of reactive percolation experiments designed to investigate the role of solute transport during the earliest stages of alteration of the mantle basement, when seawater-derived hydrothermal fluids

penetrate and interact with the sub-seafloor mantle basement. The experiments were conducted by injecting artificial seawater at four different flow rates through cores made of compressed olivine powder. The composition of the injected artificial seawater was calculated in order to model that of seawater heated up when flowing along high permeability fracture zones. Olivine was chosen as starting material to limit the effects of mineralogical heterogeneities on serpentinization reaction paths. Experiments were performed using high porosity and permeability cores in order to avoid clogging of pore network due to serpentinization reactions and thus to minimize the change of the rate of solute renewal at fluid-mineral interfaces along flow paths during experiments. The objectives of this study are to better understand the coupling between fluid flow, solute transport and chemical processes during fluid-rock interactions, its effects on the mechanisms that control outlet fluid chemistry and chemical reaction path from the pore- to the sample-scale, and their role for the serpentinization of the oceanic mantle lithosphere.

2. Experimental and analytical methods

2.1. Experimental setup

Reactive percolation experiments were carried out using the Icare Lab 3 flow-through system (Géosciences Montpellier, France) (Fig. 1). This experimental bench allows investigating water-rock interactions in confined permeable cylindrical samples of 9 mm diameter *(D)* and 20 mm length *(L)*. It includes an automatic system of fluid injection with three computer-controlled hydraulic pumps of 35 mL volume that allows maintaining a constant flow rate (Q) ($10^{-6} \leq Q \leq 2$ mL·min^{-1}) and a heated confinement cell that holds the sample at constant temperature (T) (<400 °C) (Fig. 1). The experiment pressure (P) (< 40 MPa) is controlled by a back pressure system with a hydraulic pump of 100 mL volume (Fig. 1). During experiments, the difference of fluid pressure between the inlet and outlet of the sample (0.003 < $\Delta P \leq 40$ MPa) is monitored using a differential pressure sensor Rosemount 3051 (accuracy of 0.003 MPa) coupled with two high resolution pressure sensors Keller PA-33 X (accuracy of 0.035 MPa). Experimental fluid samples of volume 3 mL are collected using a pressurized

computer-controlled syringe. Pump motion, valves and fluid sampling are operated by an in-house LabView-based software.

The four reactive-percolation experiments consisted in injecting artificial seawater (ASW) into compressed San Carlos olivine powders at different constant flow rates (Q): SC1-LQ, SC2-MQ, SC3-HQ and SC4-VHQ were performed at low ($Q = 0.24$ mL·h^{-1}), medium ($Q = 0.48$ mL·h^{-1}), high ($Q = 1.14$ mL·h^{-1}) and very high ($Q = 5.21$ mL·h^{-1}) flow rate respectively. The four experiments were performed at the same temperature ($T = 170$ °C) and pressure ($P = 25$ MPa) conditions. The permeability k of the samples (in m^2) was calculated using Darcy's law assuming laminar flow conditions:

$$k = -\frac{\mu L Q}{S \Delta P} \tag{1}$$

with Q the injection rate (in m^3/s), μ the dynamic fluid viscosity (0.197 × 10^{-3} Pa. s at 170 °C and 25 MPa for a salinity of 0.5 mol/kg (Kestin et al., 1981), and L and S the sample length (in m) and cross sectional area (in m^2) respectively. The changes in ΔP are measured continuously during the experiment. Experimental conditions and sample characteristics are summarized in Table 1.

2.2. Sample preparation

2.2.1. Olivine samples

The olivine samples are powdered San Carlos olivine compressed into a 20 mm length, 7 mm internal diameter steel tubes (Fig. 2). The composition of San Carlos olivine is Fo91 (Appendix A, Supplementary Material). Powders were obtained by grounding olivine grains of few millimeters (typically 5 mm). The grains were optically selected under a binocular microscope to eliminate those with microphases or inclusions. Then, the grains were grounded in an agate mortar, sieved and ultrasonicated three times in MilliQ water. The 100–150 µm olivine grain fractions was selected for the experiments (Fig. 2a) and introduced into the stainless steel (316 L) tubes by successive layers of ~2 mm. Each layer was compressed, using a hydraulic press, at 4.13 MPa. The process was repeated until the capsule was completely filled (Fig. 2b-c). Then, two cylindrical stainless steel (316 L) frit plugs of 2 mm thickness were emplaced on each end of the tube to seal the
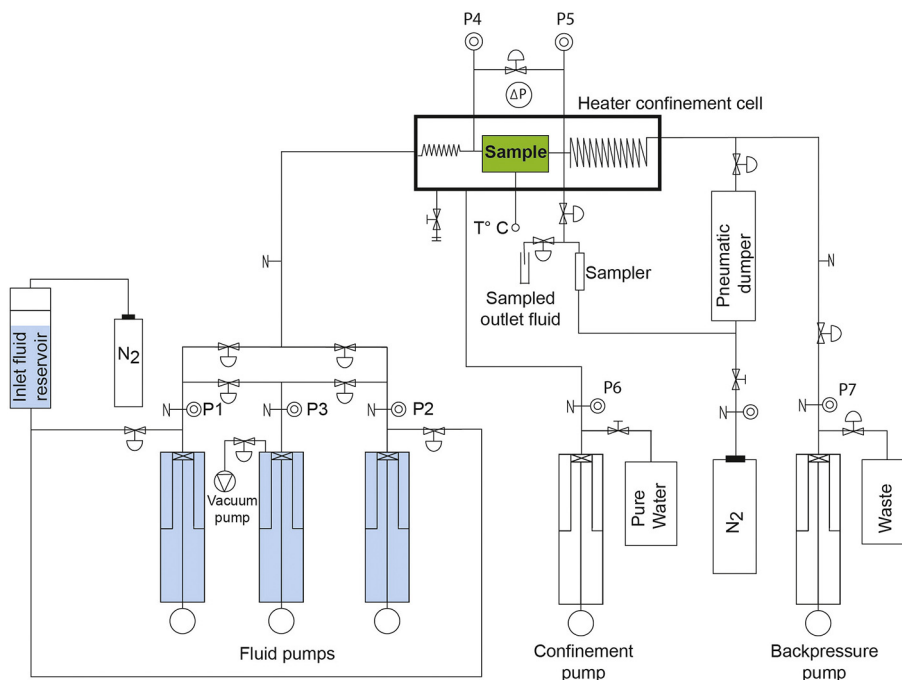

Fig. 1. Schematic diagram of the experimental flow through setup (Icare Lab 3).

Table 1
Experimental parameters of experiments SC1-LQ (low flow rate), SC2-MQ (medium flow rate), SC3-HQ (high flow rate) and SC4-VHQ (very high flow rate). The experiments were run at 170 °C and 25 MPa using artificial seawater (ASW) as injected solution.

Experiment	Flow rate	Residence time	Duration	Olivine sample	Sample diameter	Sample length	Grain size	Initial weight	Initial porosity	Peclet number	Mean fluid velocity	Permeability avg.
	$(Q = ml/h)$	(min)	$(hours)$		(mm)	(mm)	(μm)	(g)	$(\%)$		$(v = m/s)$	$(k = m^2)$
SC1-LQ	0.24	158	354	SC1	7.09	16.00	150–100	1.71 ± 0.01	19.3	0.2	8.8×10^{-6}	$5.7 \times 10^{-15} \pm 1.2 \times 10^{-15}$
SC2-MQ	0.48	77	668	SC2	7.11	15.50	150–100	1.76 ± 0.01	14.9	0.5	2.3×10^{-5}	$3.5 \times 10^{-15} \pm 2.9 \times 10^{-15}$
SC3-HQ	1.14	34	263	SC3	7.13	16.02	150–100	1.77 ± 0.01	17.4	0.9	4.6×10^{-5}	$3.3 \times 10^{-15} \pm 1.1 \times 10^{-15}$
SC4-VHQ	5.21	7	617	SC4	7.09	15.85	150–100	1.70 ± 0.01	18.8	4.0	2.0×10^{-4}	$3.7 \times 10^{-15} \pm 1.5 \times 10^{-15}$

olivine powder into the capsule. The characteristics of samples SC1, SC2, SC3 and SC4 used for experiments SC1-LQ, SC2-MQ, SC3-HQ and SC4-VHQ respectively are reported in Table 1.

2.2.2. Artificial seawater

Artificial seawater (ASW) was prepared to simulate the composition of natural seawater progressively heated at 170 °C and depleted in Mg- and Ca-rich carbonates and sulfates while penetrating the oceanic lithosphere. The ASW composition, reported in Table 2, was calculated using the EQ3/6 geochemical modelling software (EQ3/6 v.8.0,Wolery and Jarek, 2003) assuming seawater (Millero et al., 2008) was heated up to 200 °C by 50 °C steps. It was calculated up to 200 °C, i.e. slightly higher than the experimental temperature (170 °C), in order to ensure that no mineral precipitation would take place in the heated confinement cell. The ASW was made before each experiment by dissolving pure salts MgCl$_2$.6H$_2$O (Merck), KCl (Prolabo Analar Normapur), NaHCO$_3$ (Panreac), NaCl (Prolabo Analar Normapur), Na$_2$SO$_4$ (Prolabo Normapur), and CaCl$_2$ (Sigma-Aldrich) into MilliQ water. The composition of injected ASW was systematically measured together with that of outlet fluids following the protocol described thereafter; it varied little from one experiment to the other. It should be noted that traces of Fe (0.90–12.86 μmol/L) were measured in the "blank solution" when pumping the ASW through the bypass before injection. The source of Fe is probably a minor alteration of the stainless steel material used for the pumps and the circuit.

The pH value of the solution was measured with a Metrohm Titrino 848 with LL Micro glass electrode, was 7.56 at room temperature (25 °C). The pH of the solution at 170 °C, calculated using EQ3/6, was 5.8. The conductivity, measured using a conductivity meter WTW LF340 with a sensor Tetracon WTW 325 was 43.5 mS/cm.

2.3. Mineralogical characterization

The mineralogy of samples was characterized after experiments using scanning electron microscopy (SEM) coupled with energy dispersive spectroscopy (EDS) and thermogravimetric analyses (TGA).

Before analyses, the reacted olivine samples were dried under vacuum for 12 h at room temperature (25 °C) to remove the fluid that remained in pores and to avoid post-experiment fluid-rock reactions. For samples SC1, SC3 and SC4, the reacted powdered samples were recovered after sawing off one of the frit plugs. Sample SC2 was prepared as a polished section using the approach of Peuble et al. (2015a, 2015b); this technique didn't allow recovering powder samples for TGA analyses.

SEM-EDS was used for grain surface characterization and semi-quantitative chemical analyses. Analyses were performed using a FEI Quanta FEG 200 Scanning Electron Microscope (University of Montpellier, France), with an acceleration voltage of 15 kV and chamber pressure of 0.38 Torr. TGA analyses were used for identifying volatile rich minerals by the loss of weight when the sample is heated. Analyses were performed by increasing the temperature from 33 °C to 1200 °C at 2 °C.min^{-1} rate under Argon atmosphere using a SDT Q600 V20.9 (IEEM, Montpellier). The curves were calibrated by performing an automatic blank curve subtraction in order to avoid measurement artefacts such as apparent gain of weight produced by buoyancy effects.

2.4. Fluid analyses

Experimental fluid samples were collected on average every day. Each fluid sample represents the integrated concentrations of the outlet fluids over the time required for 3 mL to flow through the percolated
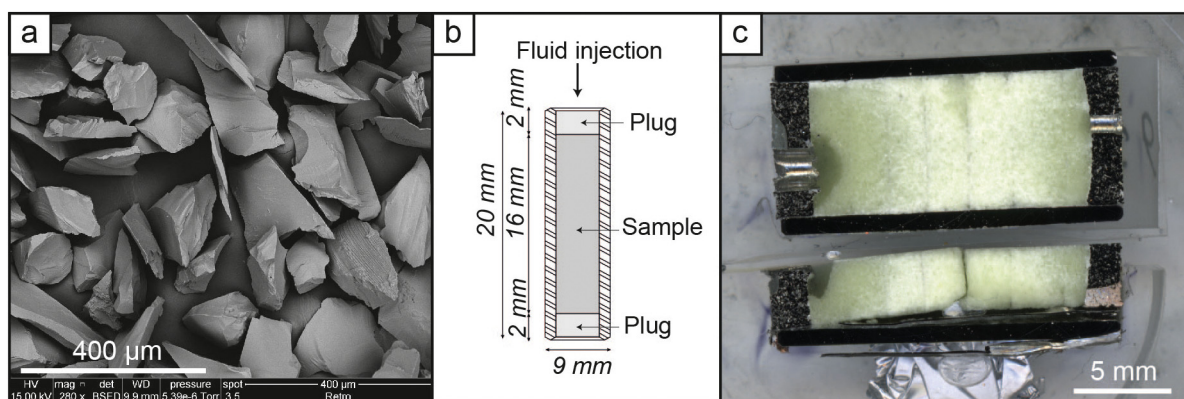

Fig. 2. (a) SEM image of starting material: ultrasonically cleaned San Carlos olivine powder. (b) Schematic diagram of sample capsule. Olivine powder is introduced in the cylindrical steel capsule (20 mm × 9 mm), which is then closed on both ends by two steel frit plugs. (c) Unreacted sample cut longitudinally. Alternating dark to light green layers are related to the filling of the steel capsule.

Table 2
Theoretical chemical composition of the starting fluid at 200 °C calculated after EQ3/6.

Element	mg/L	mmol/L
Mg	1083	44.6
Ca	128	3.2
K	340	8.7
Na	9163	398.6
Cl	16,468	464.5
SO4	1799	18.7
HCO3	47	0.8

samples: the last 12.5 h, 6.25 h, 2.63 h and 0.58 h before sampling time for experiments SC1-LQ, SC2-MQ, SC3-HQ and SC4-VHQ respectively (Appendix B. Table B.1 to B.4).

Alkalinity and pH were measured using a Methrom Titrino 848. Measurements were performed <5 min after the fluid sample was collected to minimize equilibration with the atmosphere. The pH was measured using 2 mL samples at 1:2 dilution in MilliQ water using a Metrohm LL Micro glass electrode. The alkalinity (HCO_3^-) was measured at 25 °C on the same fluid sample by acid titration with 0.01 M HCl. The reagent was added to the fluid sample in variable volume steps to a pH endpoint of 4.5. (HCO_3^-) was assumed to be equal to total alkalinity (Bischoff and Seyfried, 1978). The reproducibility and accuracy of alkalinity measurements were assessed using repeated measurements of Volvic® water. They were better than 5% and 15%, respectively. The pH accuracy was better than 3%. Values are reported in supplementary material (Appendix C).

SO_4^{-2} was analyzed using a Dionex ICS-100. Water samples were analyzed after a dilution of 500 with MilliQ water. The reproducibility and accuracy of measurements were assessed using IAPSO (seawater sample) (Summerhayes and Thorpe, 1996) and was better than 1% and 1% respectively (supplementary material, Appendix C).

Si, Fe, Mg, Ca and Na were analyzed using a Thermo Scientific ICAP 7400 ICP-OES (Géosciences Montpellier) after a dilution of 50 in acidified MilliQ water (2% HNO_3). The reproducibility and accuracy of measurements were assessed using SLRS-5 (River water sample) (NRC-CNRC) certified standard and was better than 10% and 5% respectively (supplementary material, Appendix C).

Speciation and saturation calculations of the experimental fluids were calculated using the EQ3/6 geochemical software (Wolery and Jarek, 2003). Calculations to estimate in situ pH and silica activity were performed using EQ3/6 following the method of Mccollom et al. (2016): first, fluid speciation was calculated at 25 °C using the fluid composition and pH measured at room temperature adjusting for charge balance with Na^+, then, the total dissolved Na^+ calculated at 25 °C was used with other measured concentrations to calculate the fluid speciation at 170 °C adjusting for charge balance with H^+ in order to determine the in situ pH.

All calculations were performed using a data base of thermodynamic parameters for 25 MPa. The data base was generated using SUPCRT92 (Johnson et al., 1992). It includes all minerals and inorganic aqueous species in the SUPCRT92 data base for the system Mg-Ca-Fe-Si-Na-Cl-O-H. SUPCRT92 incorporates thermodynamic data from Helgeson et al. (1978) for minerals, and Shock and Helgeson (1988) and Shock et al. (1989, 1997) for dissolved inorganic aqueous species. Activity coefficients for aqueous species were calculated using the B-dot equation (Helgeson et al., 1981).

3. Results

3.1. Characteristics of the reacted samples: permeability and mineralogy

Permeability stayed constant during the four experiments (Table 1). Experimental samples had high porosities (14.9–19.3%) at the start of the experiments. The lack of permeability variations indicates that changes in mineralogy during the experiments were not large enough in volume to block porosity and flow paths.

At the end of the four experiments, the reacted samples generally preserved the initial green colour of olivine, with locally white patches (Fig. 3), suggesting that changes in the mineralogy of the samples were minor. They show however dark brown patches at the inlet and outlet of the capsule and black spots peppered throughout the samples indicating possible precipitation of oxides. Trace Fe concentrations in injected fluids may have favored oxide precipitation at the sample inlet. At the micro-scale, mineral alteration features become more noticeable. Mineral deposits were identified by SEM-EDS on olivine surfaces in the four reacted samples (Fig. 4). Olivine appears covered by 2 to 3 μm patches of fluffy light grey deposits bounded by dark grey lines (Fig. 4b). At the nano-scale, these fluffy deposits present different textures in the four reacted samples (Fig. 4c-f).

Sample SC1-LQ (lowest flow rate experiment) shows small (<50 nm) nodular aggregates localized along the primitive discontinuities of the olivine grains (Fig. 4c). These textures are similar to that described by Lafay et al. (2012) and Ogasawara et al. (2013) as incipient chrysotile. Sample SC2-MQ (medium flow rate experiment) displays also nodular deposits but slightly bigger than in Sample SC1-LQ (Fig. 4d). Similar nodular textures were described by Andreani et al. (2009) as proto-serpentine. Silica-rich zones were also observed (Fig. 5). They have a characteristic length of approximately 10 μm and SEM-EDS analyses indicate low Mg/Si ratio (~ 0.3) compared to olivine (Mg/Si = 1.8). A few calcite grains were also identified at the sample inlet. Sample SC3-HQ (high flow rate experiment) shows an assemblage of fibrous filaments (Fig. 4e). In some places, filaments follow a preferential orientation; they have textures similar to those described by Lafay et al. (2012) as indicating incipient stages of chrysotile formation. Elsewhere, filaments are randomly oriented forming honeycomb textures similar to those described by Luhmann et al. (2017) and interpreted by these authors as secondary mineralization features. Because of the nature of the samples (powder), we could not determine a possible relation between the texture and the flow direction. Sample SC4-VHQ (highest flow rate experiment) also displays fibrous filaments on olivine surfaces (Fig. 4f). These fibrous filaments have textures similar to those observed in Sample SC3-HQ but they are less prominent (smaller and less abundant).

TGA analysis indicates minor changes in the composition of samples during experiments with a total weight loss of <1% for analyzed samples SC1-LQ, SC3-HQ and SC4-VHQ (Fig. 6). All samples show a steady decrease in mass with increasing temperature up to 1000 °C in relation to progressive dehydration of the rock samples. Weight loss increases for decreasing flow rates suggesting that secondary phases were more abundant when flow rate was slower. Small steps in the weight loss curves can be used to identify these secondary phases (Földvári, 2011). The first step at 100 °C indicates the loss of molecular water. A second step is observed between 600 °C and 700 °C in all samples (Fig. 6). It is particularly marked in Sample SC1-LQ (− 0.92 wt%) where it occurs between 580 °C and 723 °C. It overlaps the expected range of temperature for the dehydration of serpentine (550–750 °C, Godard et al., 2013; Földvári, 2011; Lafay et al., 2012; Viti, 2010). This second step occurs at higher temperature and becomes progressively less pronounced as flow rate increases in samples SC3-HQ (− 0.76 wt%, 638 °C) and SC4-VHQ (− 0.61 wt%, 653 °C. Very small variations in the weight loss curves are observed around 330 °C for Sample SC1-LQ and around 340 °C for Sample SC4-VHQ. It could relate to the presence of small amounts of neoformed brucite which dehydration temperature ranges between 350 and 450 °C (Földvári, 2011).

3.2. Fluid chemistry of the outlet fluids

Outlet fluids have high pH and low alkalinity compared to inlet fluids (Fig. 7; Appendix B. Tables B.1 to B.4). The increase in pH indicates dissolution of silicates (here olivine) (Gislason and Oelkers, 2003; Seyfried et al., 2007) and the decrease in alkalinity suggests carbonate trapping
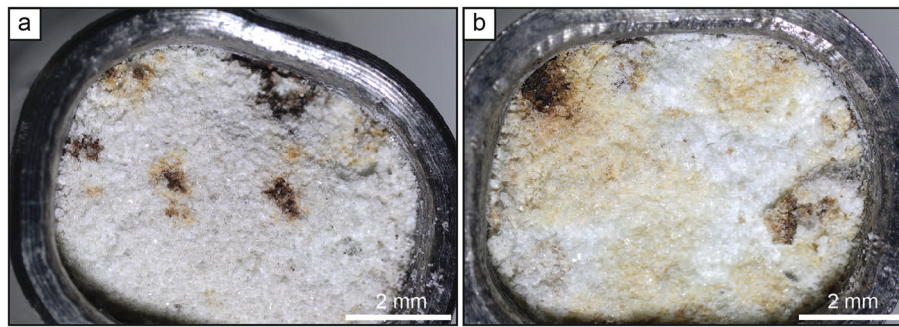
Fig. 3. Binocular photo of the (a) inlet and (b) outlet of sample SC1-LQ.

and/or changes in the carbonate speciation. Outlet fluids display similar in situ pH values from one experiment to the other (~6.1) suggesting that the outlet fluids are buffered by the same mineral assemblage.

These pH values calculated at 170 °C indicate that, similar to inlet fluids (in situ pH_{ASW} ~ 5.8), all outlet fluids are slightly alkaline (higher that neutral pH at 170 °C = 5.68 (Bandura and Lvov, 2006) calculated at
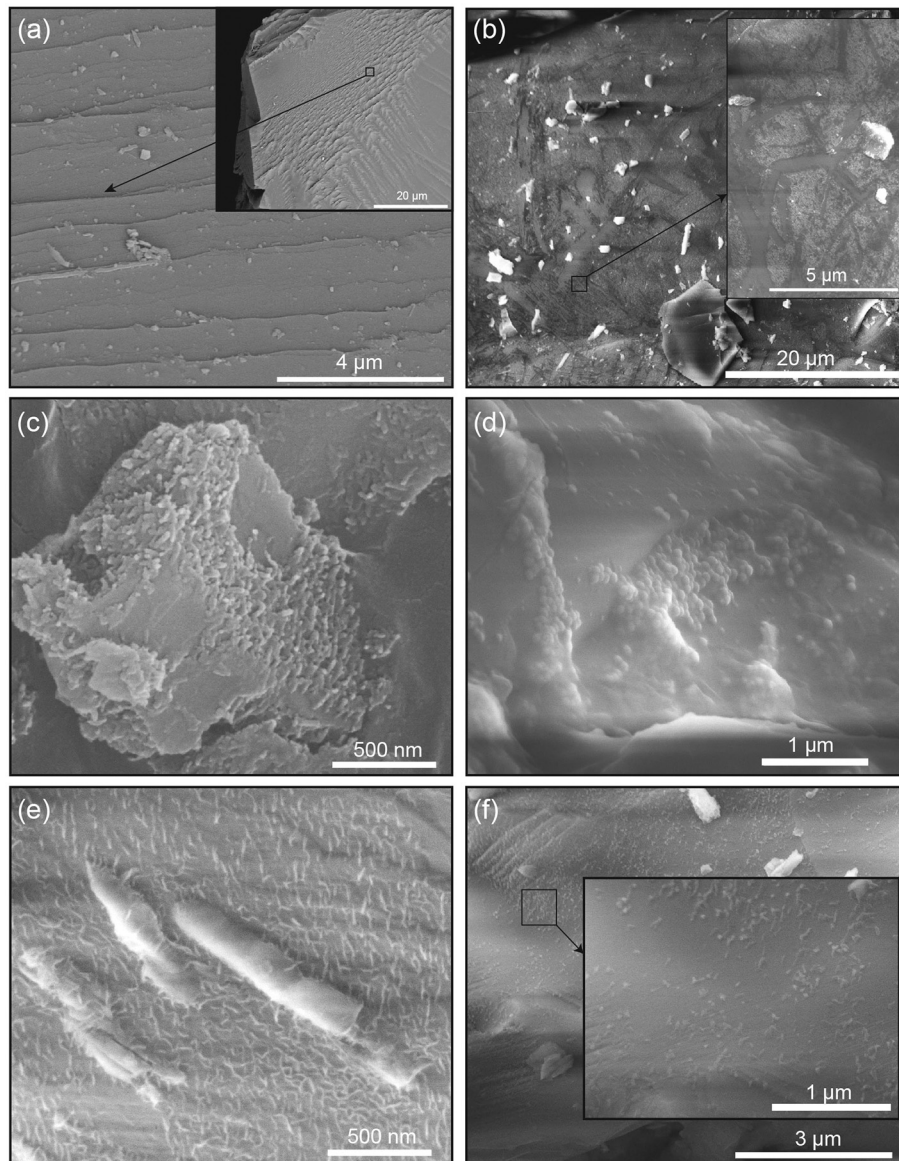
Fig. 4. SEM images of the surface of unreacted and reacted olivine grains. (a) The surface of unreacted olivine grains is rough and uneven: grains were mechanically cracked, mainly along crystallographic planes, during sample preparation (powdering, compression on olivine layers during capsule filling) and nano olivine grains are typically observed on these surfaces. (b) Reacted olivine surfaces are covered by 2–3 μm large patches of a fluffy light grey deposit bounded by dark grey lines (Sample SC3-HQ). Small undissolved olivine grains (white) are observed on the surface and are sometimes covered by these deposits. At nano-scale, the fluffy deposit has different textures in the three reacted samples: (c-d) Nodular aggregates developed on the reacted olivine surface in sample SC1-LQ and SC2-MQ respectively. (e-f) Assemblage of fibrous filaments evolved in sample SC3-HQ and SC4-VHQ respectively.
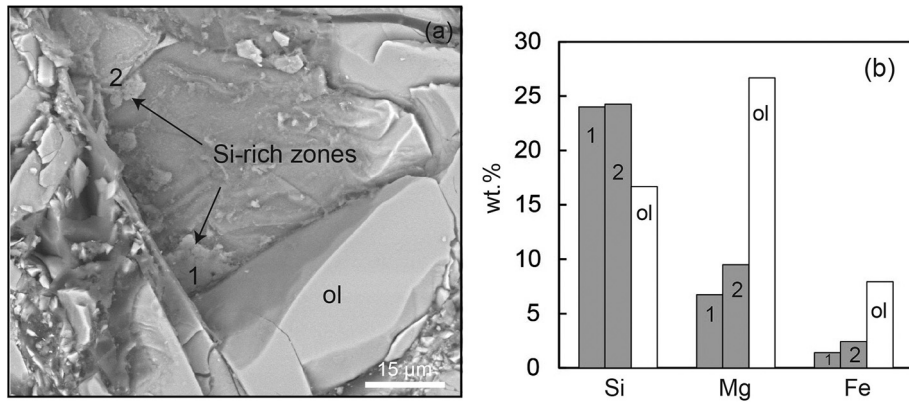
Fig. 5. SEM images of Sample SC2-MQ. (a) Silica rich zones, 1 and 2, were identify by SEM-EDS. (b) SEM-EDS analysis (in wt%) on the silica rich zones and olivine (ol).

25 MPa). In contrast to pH, carbonate alkalinity displays a broad range of values from one experiment to the other. Carbonate alkalinity of outlet fluids is overall low during experiments SC1-LQ (27.5–30.5 mg/L) and SC2-MQ (27.5–33.0 mg/L). It displays highly scattered values (29.9–47.0 mg/L) during experiment SC3-HQ but no significant trends. In contrast, carbonate alkalinity of outlet fluids during experiment SC4-VHQ increases with time (27.5–37.2 mg/L); it increases also with increasing pH, as expected for a solution close to neutral pH becoming more alkaline (Zeebe and Wolf-Gladrow, 2001).

The outlet fluid composition in the cations dominant in olivine (Si, Mg, Fe) and in ASW (Mg, Ca) varies with time and from one experiment to the other (Fig. 8, Appendix B. Tables B.1 to B.4) indicating differences in the extent and kinetics of dissolution and precipitation reactions. Low Q (SC1-LQ and SC2-MQ) and high Q (SC3-HQ and SC4-VHQ) experiments show distinct time series. Experiments SC1-LQ and SC2-MQ are characterized by a sharp and selective increase in Si in the outlet fluids (up to 0.24 mmol/L) followed by a sharp decrease during the early stages of the experiments (⟨200h⟩). Mg, Ca and Fe outlet fluid concentrations are relatively constant during these experiments except for an increase in Mg (up to 41.5 mmol/L) and Ca (up to 3.4 mmol/L) between 90 and 112 h during experiment SC1-LQ. In contrast, experiments SC3-HQ and SC4-VHQ are characterized by a steady decrease in Si concentrations in the outlet fluids with time. Overall, Mg, Fe and Ca concentrations decrease with time in the outlet fluids during experiment SC3-HQ. During experiment SC4-VHQ, Mg, and Ca concentrations are more variable but the overall trend is apparent steady state whilst Fe shows a strong increase in composition during the first 400 h of the experiment (up to 45.1 μmol/L).

Sharp increases in all cation concentrations in outlet fluids are commonly observed during the early stages of reactive-percolation experiments using sintered and compressed mineral powders (e.g., Andreani et al., 2009; Godard et al., 2013; Peuble et al., 2015a). These enrichments are attributed to the fast dissolution of the small mineral fragments

(characterized by their large reactive surface area) produced during compression of the μm-olivine grains. Such trends are not observed in this set of experiments. The selective Si enrichment observed during
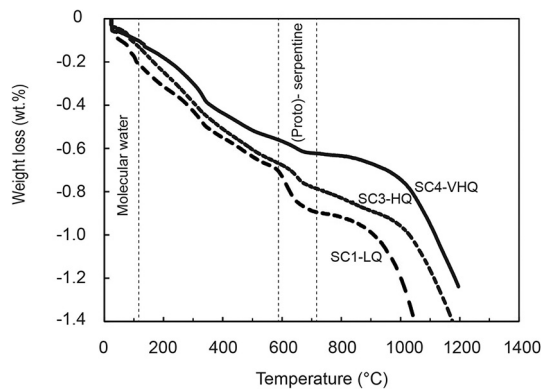

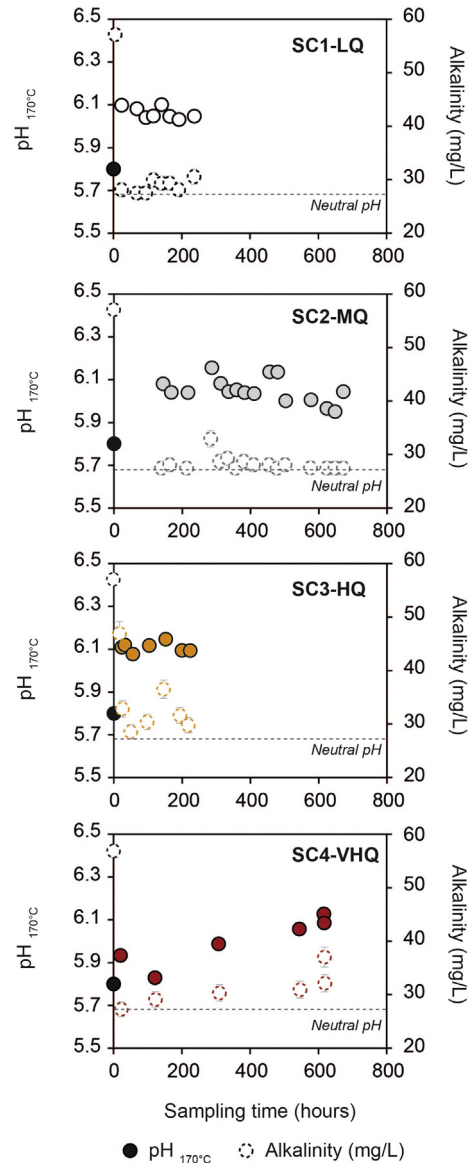**Fig. 6.** Thermogravimetric analysis of Samples SC1-LQ, SC3-HQ and SC4-VHQ.

Fig. 7. pH calculated at 170 °C and alkalinity measured at 25 °C of the outlet fluids for SC1-LQ, SC2-MQ, SC3-HQ and SC4-VHQ.
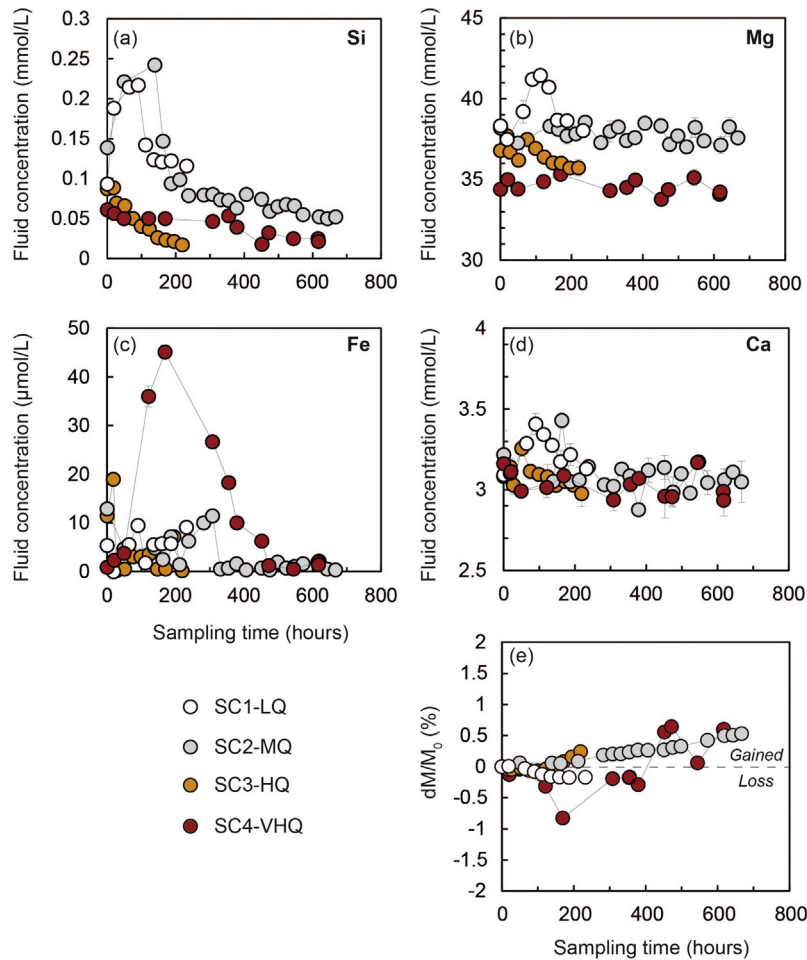
Fig. 8. (a-d) Si, Mg, Fe and Ca concentrations (mg/L) of the outlet fluids as a function of time of sampling (h) for experiments SC1-LQ, SC2-MQ, SC3-HQ and SC4-VHQ. (e) Total mass changes in the reacting samples with time on a volatile-free basis. Mass balances (M_{inlet} – M_{outlet}) were calculated using fluid time series assuming all cations occurred as oxides. Positive values indicate that samples gained mass during experiments (mineral trapping). Negative values indicates cationic loss compared to the initial sample mass, but does not preclude an actual increase in the mass of the samples during experiments as H_2O and CO_2 trapping associated to the formation of hydrous phases and carbonates are not taken into account in these calculations.

the early stages of experiments SC1-LQ and SC2-MQ suggests that preferential dissolution of smaller grains did occur but that the kinetics of the processes controlling Mg-trapping were faster compared to those controlling Si-trapping in these experiments. The absence of such transient cationic enrichments in the early stages of experiments SC3-HQ and SC4-VQ suggests an alternate coupling mechanism between dissolution/precipitation kinetics and transport at high flow rates.

As illustrated on Fig. 8, the mass of Si, Mg, Fe and Ca oxides lost and/ or gained calculated using fluid time series can provide a first estimate (on a volatile-free basis) of the mass changes in the reacting samples (e.g., Godard et al., 2013). Mass balances are calculated assuming that fluid concentrations at the sampling time are representative of the outlet fluid composition between sampling. The four experiments record variations in the total mass of reacted samples but these changes are small. Sample SC1-LQ shows a progressive decrease in mass with time down to 0.16 wt% relative to its initial mass whilst samples SC2-MQ and SC3-HQ indicate an increase in mass of up to 0.50 wt% relative to its initial mass for experiment SC2-MQ (the longest duration). The overall trend is difficult to evaluate for sample SC4-VHQ: the strong scatter in the calculated mass trends indicates that the assumption that analyzed fluid compositions are representative of the average composition of fluids between sampling is undoubtedly not correct for experiment SC4-VHQ. Nevertheless, we note that similar to sample SC2-MQ, sample SC4-VHQ shows the largest change in mass. Experiment SC4-VHQ was the second longest experiment suggesting that, to the first order, the

total mass of dissolved and precipitated minerals at the end of experiments is proportional to their duration (Fig. 8).

In an attempt to constrain the precipitation and dissolution processes that control the sample mass variations, we calculated the saturation indexes in the outlet fluids using the EQ3/6 geochemical software using the 25 MPa thermodynamic database generated for this study. The saturation index Ω is defined as

$$\Omega = \frac{IAP}{K} \tag{2}$$

where *IAP* is the ion activity product, and *K* is the equilibrium constant. When log (Ω) is negative for a given mineral, the solution is undersaturated and can potentially dissolve this mineral. When it is positive, the solution is saturated and this mineral has the potential to precipitate, provided nucleation occurs and kinetics are favorable.

As illustrated on Fig. 9, olivine is under-saturated in the four experiments and is thus expected to dissolve. It should be noted that olivine saturation indexes are overall the lowest for high flow rate experiments, SC3-HQ and SC4-VHQ, suggesting that disequilibrium toward olivine is more efficiently maintained during these experiments compared to the others. Outlet fluids are saturated for serpentine (chrysotile) and hematite, indicating chemical conditions favorable for their precipitation. Magnetite saturation indexes oscillate around zero whilst brucite saturation indexes are slightly negative (close to zero) in the four
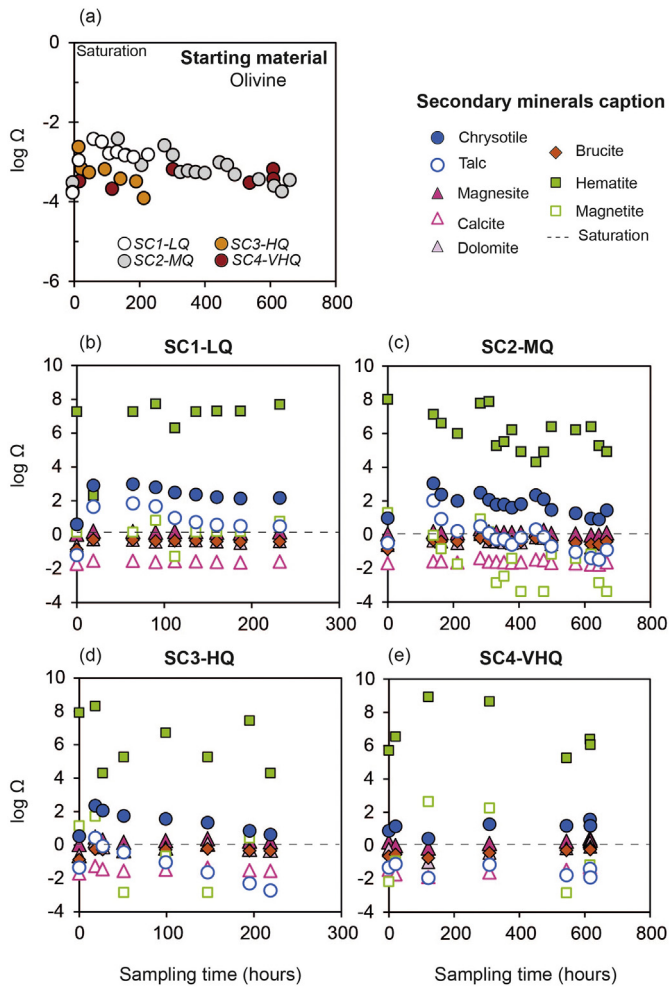
Fig. 9. Saturation index (Ω) for outlet fluids during experiments SC1-LQ, SC2-MQ, SC3-HQ and SC4-VHQ. Saturation indexes were calculated at 170 °C and 25 MPa using EQ3/6 (Wolery and Jarek, 2003). (a) Saturation index of the primary mineral (olivine) versus sampling time; (b-e) Saturation index calculated for chrysotile, talc, magnesite, calcite, dolomite, brucite, hematite and magnetite for each experiment.

experiments. At the calculated pH conditions, outlet fluids are slightly too Fe- and Mg-poor to be systematically saturated relative to magnetite and brucite respectively; we cannot preclude however that percolating fluids did not reach locally saturation for these minerals, in particular in the vicinity of dissolving olivines. Talc saturation indexes in outlet fluids are positive for experiment SC1-LQ, they decrease with time (from positive to negative) during experiments SC2-MQ and SC3-HQ, and are negative for experiment SC4-VHQ. This suggests that the processes controlling silica activity in our experiment is, at least in part, related to flow rate. This may imply a relation to transport properties and/or to the actual water/rock ratio. Thermodynamic modelling using the EQ3/6 code were run at experimental conditions assuming equilibrium to test the effect of effective water / rock ratio on the secondary mineralogy (Appendix G. Fig.G1). Results indicate that brucite precipitates preferentially for low water/rock ratios. Consequently, we infer that its formation would be favored in low flow experiments; this would in turn explain the slightly higher Si activity in the outlet fluids for these experiments (Fig. 8a). Saturation indexes of carbonates are slightly negative (calcite) or close to zero (magnesite and dolomite) for all experiments except for huntite ($Mg_3Ca(CO_3)_4$). Huntite saturation indexes range between 125 and 127 for all experiments (Appendix D. Table D). It is worth to note that, in the field, the precipitation of huntite is also typically associated to low temperature hydrothermal alteration of ultramafic basements (e.g., Stanger and Neal, 1994).

4. Discussion
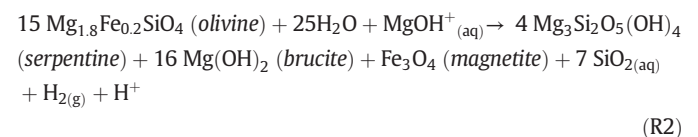
4.1. Flow rate and fluid-rock reaction paths

Post-experiment characterization shows minor changes in the overall composition and structure of reacted sample suggesting that serpentinization kinetics was slow compared to the duration of the experiments. Nevertheless, outlet fluid composition time series (Fig. 9) and the occurrence of serpentine-type minerals and minor carbonates coating the olivine surface (Fig. 4) indicate that fluid-rock reactions occurred. All measured inlet and outlet fluid compositions plot in the domain of stability of serpentine in the $Mg^{2+}/(H^+)^2$ versus SiO_2 activity diagram (Fig. 10). This denotes that 1) the fluid is undersaturated with respect to olivine and 2) the neoformed serpentine is buffering the composition of fluids throughout the experiments. This implies that serpentine precipitation occurs close to equilibrium. Furthermore one observes that the composition of outlet fluids tends toward similar $aMg^{2+}/a(H^+)^2$ values ranging from 9.7 to 10 suggesting that a steady-state regime of mass transfer is achieved and controls the pH and the Mg activity. This steady-state is achieved in a few hours for all experiments except for experiment SC4-VHQ (Table B.4 (Appendix B); Fig. 10a-b) for which it is achieved after 300 h. This is a first indication that the flow rate is a controlling parameter of the effective fluid-mineral mass transfer rate.

Additionally, we observe two trends in the evolution of SiO_2 activity. Outlet fluid time series of low Q experiments SC1-LQ and SC2-MQ show first an increase in SiO_2 activity then a decrease associated with a constant $aMg^{2+}/(H^+)^2$. At the opposite high Q experiments SC3-HQ and SC4-VHQ are characterized by a decrease of the SiO_2 activity which starts since the beginning for the experiment with the highest value of Q. These distinct behaviors suggest the development of different reaction paths and thus the predominance of different mass transfer mechanisms.

Secondary phases were too few and too small to be analyzed, which precluded evaluating precisely the amount of dissolved and precipitated phases using the fluid-time series. The reactions for the lowest values of Q and for the highest values of Q were thus determined on the basis of (1) our observations of the reacted samples and fluid time series which suggest olivine dissolution and precipitation of oxides, serpentine-type hydrous phases and minor carbonates and (2) the following assumptions for the composition of the precipitated phases: (i) serpentine, and brucite when present, do not incorporate Fe. (ii) The neoformed oxide is magnetite. (iii) All carbonates have the composition of huntite.

Magnetite was hypothesized to be the Fe-bearing secondary phase for these calculations, as it is the main oxide formed during serpentinization in natural conditions (e.g., Bach et al., 2004). Reactions written assuming that the Fe-bearing secondary phase is hematite (oxidizing conditions) are overall similar to those described thereafter (Appendix E). It should be noted also that several studies of experimental serpentinization (e.g., Godard et al., 2013; Marcaillou et al., 2011) and oceanic serpentinites (e.g., Andreani et al., 2013) indicate that incipient serpentinization can produce Fe-bearing serpentines. Unfortunately it was not possible to characterize the chemical composition of the neoformed proto-serpentine aggregates in our experiments because they were too small (<1 μm). Thus, hypotheses (i) and (ii) may lead to overestimating the fraction of secondary oxides (up to 13%).

The first type of serpentinization reaction results in Mg trapping and/or release of Si (Fig. 11a) and produces serpentine-type minerals having nodular textures (Fig. 4c-d). This reaction characterizing the low Q experiments SC1-LQ and SC2-MQ can be written as:
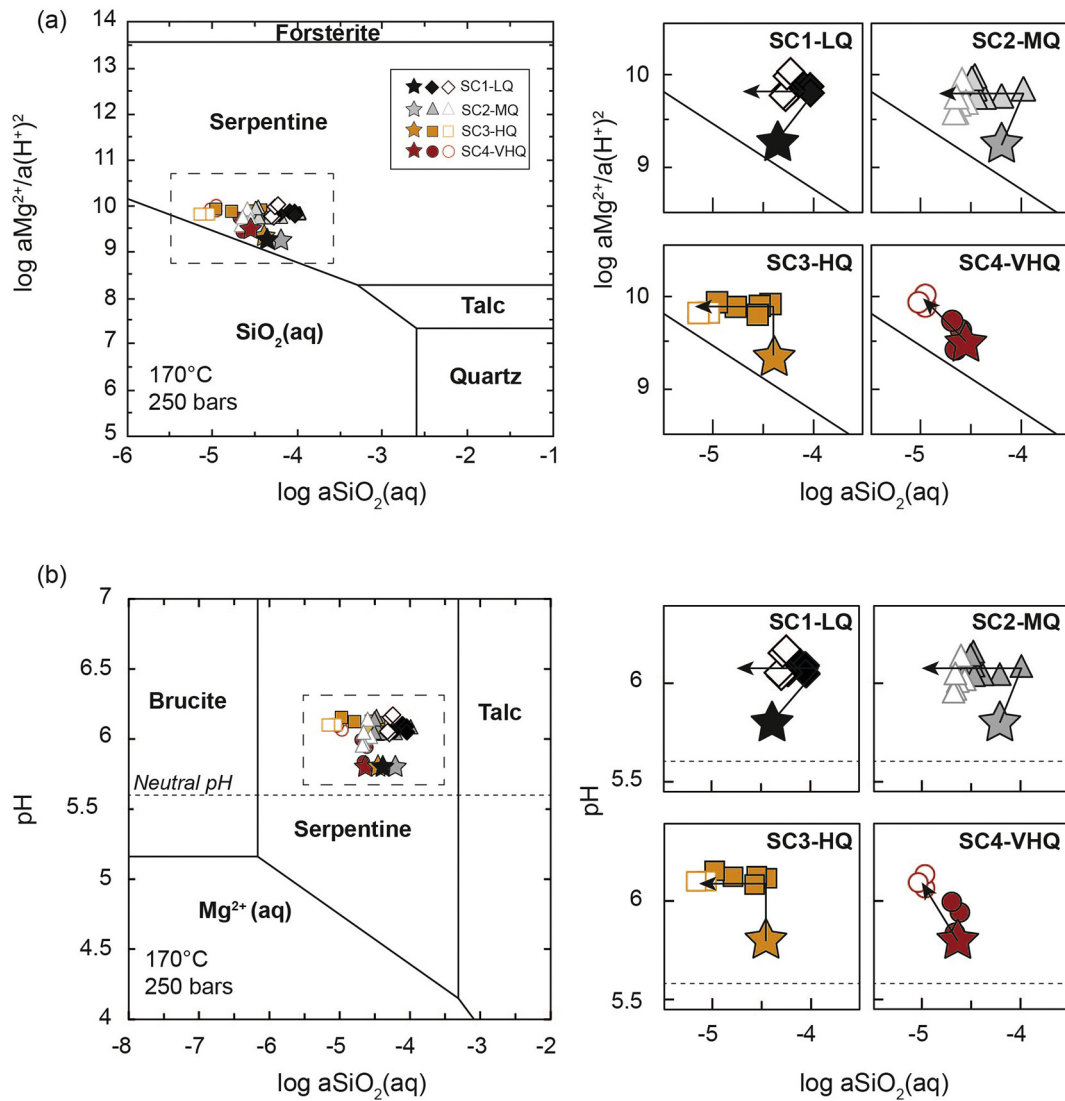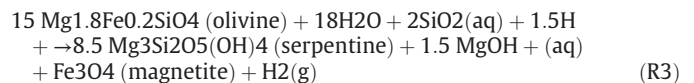
$$15\ Mg_{1.8}Fe_{0.2}SiO_4\ (olivine) + 25H_2O + MgOH^+_{(aq)} \rightarrow 4\ Mg_3Si_2O_5(OH)_4$$
$$(serpentine) + 16\ Mg(OH)_2\ (brucite) + Fe_3O_4\ (magnetite) + 7\ SiO_{2(aq)}$$
$$+ H_{2(g)} + H^+$$

$$(R2)$$

Fig. 10. (a-b) Activity-activity diagrams illustrating equilibrium for the MgO-SiO₂-H₂O-NaCl system at 170 °C and 250 bars calculated using GWB (Bethke, 1996). The filled stars represent the initial fluid (ASW) for each individual experiment. The filled symbols indicate beginning of the experiment (160 h first hours for SC1-LQ, 400 h first hours for SC2-MQ, 150 h first hours for SC3-HQ, and 309 h first hours for SC4-VHQ). The open symbols indicate the end of the experiment (145 h last hours for SC1-LQ, 261 h last hours for SC2-MQ, 72 h last hours for SC3-HQ and 309 h for SC4-VHQ). (a) All fluid samples denote increase in aMg^{2+}/a(H$^+$)^2 compared to the initial fluid solutions. SC1-LQ and SC2-MQ shows increase in the aSiO₂ (aq) compared to the ASW on the first hours to then decrease the activity during the last hours. SC3-HQ and SC4-VHQ shows decrease in aSiO₂ (aq) for all fluid samples compared to the ASW. (b) All fluid samples denote an increase on pH.

Concomitant Si enrichment in fluids with Mg trapping has been observed by Godard et al. (2013) during reactive percolation experiments with injection of artificial seawater into olivine cores at low flow rates. Increase in Si concentrations in fluids were also documented during closed-system serpentinization experiments (batch reactors, gold cell hydrothermal equipment) when reacting artificial seawater with olivine (Allen and Seyfried, 2003; Berndt et al., 1996; Klein et al., 2013) and with peridotite (Allen and Seyfried, 2003; Janecky and Seyfried, 1986; Klein et al., 2015; Seyfried et al., 2007; Seyfried and Dibble, 1980). When pyroxene was present in the primary mineral assemblage, selective increase in SiO₂(aq) was ascribed to pyroxene dissolution (e.g., Klein et al., 2015) but Si enrichment in fluids was documented also when only olivine was present (e.g., Mccollom et al. (2016) in seawater and Okamoto et al. (2011) in pure water). It is worth noticing that all these experimental studies indicate that increase in Si concentrations occur essentially during the earliest stages of serpentinization.

The second type of serpentinization reaction favors Si-trapping and release of Mg in the fluid, while produces filament-type proto-serpentine (Fig. 4e-f). It characterizes experiment SC4-VHQ (Fig. 11d):

$$15\ Mg_{1.8}Fe_{0.2}SiO_4\ (olivine) + 18H_2O + 2SiO_2(aq) + 1.5H$$
$$+ \rightarrow 8.5\ Mg_3Si_2O_5(OH)_4\ (serpentine) + 1.5\ MgOH + (aq)$$
$$+ Fe_3O_4\ (magnetite) + H_2(g) \qquad (R3)$$

The textures of the secondary products are comparable to those reported by Luhmann et al. (2017) for reactive percolation experiments during which artificial seawater and Si-rich artificial seawater were injected into pyroxene-bearing dunite cores. Flow injection rates during the Luhmann et al. (2017) experiments are similar to experiment SC3-HQ. The variations in outlet concentrations in Si and Mg for the Si-rich artificial seawater experiments of Luhmann et al. (2017) are remarkably similar to those of experiment SC4-VHQ suggesting a control of inlet fluid compositions on the reactivity of the fluid-rock system, in addition to transport.

Serpentinization reaction paths (R2) and (R3) indicate strong feedbacks between mineral reactions and fluid compositions, and

emphasize the importance of pH variations during serpentinization reactions as previously noted by Janecky and Seyfried (1986). The first type of serpentinization reaction traps Mg and decreases pH (R2) whereas the second traps Si and increases pH (R3) as observed in the course of the low Q and the high Q experiments respectively. Carbonate formation will increase or hamper these trends as it releases protons in the solution and will decrease both pH and alkalinity:

$$CaOH^+_{(aq)} + 3\ MgOH^+_{(aq)} + 4\ CO_{2(aq)} \rightarrow CaMg_3(CO_3)_4\ (Huntite) + 4H^+$$

(R4)
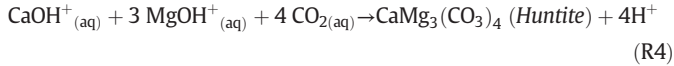
However, it must be noted that the first volume of fluid sampled at the outlet systematically display higher pH values compared to those of the inlet fluid for SC1-LQ, SC2-MQ and SC3-HQ. This indicates that the mechanism(s) governing proton trapping predominate(s) in the early stages of these experiments.

These divergences in chemical trends from one experiment to the other as well as the comparison to other experiments performed for similar conditions suggest that reaction paths and kinetics during incipient serpentinization are, at least partially, controlled by solute transport. The dimensionless Péclet number (Pe) is often used for evaluating whether advection or diffusion is the dominant transport mechanism for chemical species in a porous media (e.g., Steefel and Maher, 2009). We calculated the values of Pe corresponding to the four reactive percolation experiments as:

$$Pe = \frac{v\lambda}{d}$$

(3)

with v the mean fluid velocity, d the diffusion coefficient and λ the characteristic length at which the process is considered. The mean fluid velocity (m/s) was defined here as the velocity distribution of the fluid in the void space, and calculated as $v = Q/\varphi S$ with Q the flow rate (m^3/s), φ the porosity and S the cross-section of the sample (m^2). The characteristic length λ was set to be that of the average pore size calculated from SEM images, i.e. 10^{-4} m. Diffusion was set to 5×10^{-9} $m^2.s^{-1}$ (Philibert, 2005). The calculated Pe values and mean velocity v values are reported in Table 1. By definition, transport is advective for $Pe >> 1$ and diffusive if $Pe << 1$. As expected, the calculated Pe-numbers increase with Q from

experiment SC1-LQ ($Pe = 0.2$) to experiment SC4-VHQ ($Pe = 4$). However, these values fall into the range [0.1, 10] in which both diffusion and advection are active mechanisms of solute transport. Yet these values indicate that in average advection is about 20 times more effective for experiment SC4-VHQ than for experiment SC1-LQ. Though, the distribution of the Pe values at pore scale does cover a very large spectrum that inherits from the distribution of the fluid velocity that typically covers several orders of magnitude in such porous media (see for examples Gjetvaj et al., 2015 and Siena et al., 2015).

Yet, for this range of Pe values, the relation between the type of reaction and the transport regime (from diffusive-dominant to advective-dominant) it not straightforward as illustrated in Fig. 11. In the following section, we will discuss the possible coupling and/or feedback effects between the kinetics of olivine dissolution, the mechanisms driving secondary mineral precipitation and the hydrodynamical renewal of the solutes at the mineral interface.

4.2. Kinetics- versus transport-controlled fluid-rock reaction path scenarios

In order to interpret the chemical trends observed during the olivine-seawater reactive percolation experiments, the mechanisms driving fluid-rock reactions are often described as a four-steps process (Morse and Arvidson, 2002; Ruiz-Agudo et al., 2014): (1) flow and transport of chemical species to the olivine surface, (2) dissolution of olivine, (3) transport of secondary chemical products to the locus of precipitation and (4) precipitation of secondary minerals. Each step is favored or hindered by different hydrodynamic and chemical processes.

Step (1) and (3) are directly related to the structural and hydrodynamic properties of the reacting porous media. First, the surface of minerals accessible to fluids, or the reactive surface area, is structurally restricted in porous media, in particular when compared to uncompressed powdered samples from which most of the thermodynamic and kinetics data available in the literature are measured, thus resulting in an overestimate of the serpentinization rate when applied directly to model natural systems (e.g., Malvoisin and Brunet, 2014). The permeability and the distribution of the fluid velocities, two parameters related to the pore structure variability, are also identified as controlling the transport of solutes to and from the surface of minerals during serpentinization (Farough et al., 2016; Godard et al., 2013; Luhmann
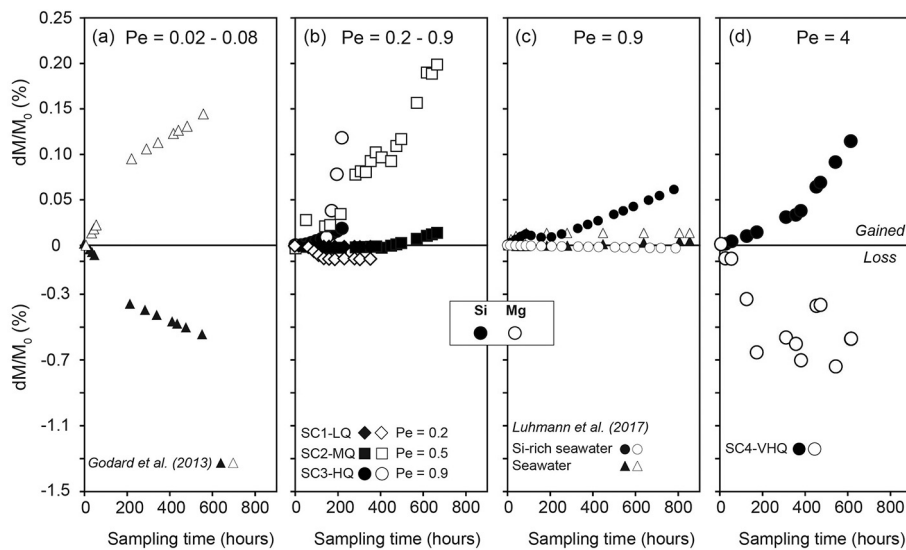

Fig. 11. (a–d) Mass of Silica (Si) and Magnesium (Mg) loss and/or gained compared to the initial mass by the four reacted samples versus sampling time. Solid symbols indicate Si and open symbols indicate Mg. (a) Low Peclet numbers ($Pe = 0.02$–0.08): Results of Godard et al. (2013) run at similar conditions of temperature (190 °C) and fluid composition (seawater) and initial sample conditions (olivine). The Peclet number was determined for a pore length of 50 µm. (b) Peclet number between 0.2 and 0.5: Results of experiment SC1-LQ ($Pe = 0.2$), SC2-MQ ($Pe = 0.5$) and SC3-HQ ($Pe = 0.9$). (c) Peclet number between 0.2 and 0.9: Results of Luhmann et al. (2017) run at similar conditions as the present experiments. Triangles shows experiments run under artificial seawater at 150 °C. Circles shows experiments run under Si-rich seawater at 200 °C. The range of Peclet number was determined for a pore length of 20 µm ($Pe = 0.2$) and 100 µm ($Pe = 0.9$). (d) High Peclet number ($Pe >> 1$): Results of experiment SC4-VHQ ($Pe = 4.0$).

et al., 2017). Permeability is controlled mainly by the flow path tortuosity and the overall connectivity of the pore network. Permeability can be noticeably altered depending on the volume and the localization of the dissolution and precipitation reactions, specifically for low porosity systems close to the percolation threshold as evidenced in carbonate dissolution/precipitation experiments for instance (e.g. Luquot and Gouze, 2009). Indeed, fast decrease of permeability was measured during serpentinization experiments of low porosity of the initial material (e.g., Andreani et al., 2009). Conversely, the four experimental samples used in this study displayed similar high initial porosity and permeability values and no noticeable changes of permeability was measured during experiments indicating that alteration of the connected pore structure resulting from fluid-rock reactions were negligible (Table 1).

Conversely, for a well-connected network of pores, the pressure gradient along the flow paths is almost constant. Thus the average (laminar) velocity along a given flow path is linearly proportional to the macroscopic flow rate and scales locally as the square of the pore diameter. Furthermore the velocity profile across a given section of a given flow path is parabolic (Poiseuille flow). This means that the thickness of the layer, at the surface of the mineral, for which the transport is dominantly diffusive (i.e. low value of the local Pe number) depends on the local hydraulic diameter and on the macroscopic flow rate (Fig. 12). The diffusion-dominated zones (diffusive layers and dead-ends) in which the mixing of the solutes is maximum, such increasing the probability of reaction compared to advection-dominated zone, control the (relative) localization of the reactions, i.e. steps 2 and 4.

These considerations imply that 1) large variability of the diffusion-dominated zone is expected in heterogeneous porous media, 2) the fraction of diffusion-dominated zones increases at low flow rate and 3) a redistribution of the diffusion-dominated zones can be triggered by the dissolution-precipitation processes while inducing negligible changes in the sample permeability. Furthermore these dissolution-precipitation processes can create dead-ends where the fluid is quasi-immobile. These mechanisms have been observed in the course of experimental dissolution of sedimentary rocks (e.g., Gouze and Luquot, 2011; Noiriel et al., 2007). In the case of the four experiments discussed here, the distribution of fluid velocities is the dominant transport parameter that changes from one experiment to the other. Accordingly, the difference between the results for these experiments must be investigated in terms of local changes induced by the different the flow regimes.

The mechanisms of dissolution (Step 2) and precipitation (Step 4) have been thoroughly investigated for ultramafic water-rock systems (e.g., reviews of Oelkers (2001) and Crundwell (2014), Rimstidt et al., 2012 and references therein). These studies showed the role of pH in controlling olivine dissolution kinetics: in acid solutions, olivine dissolution rate is fast and proportional to the activity of protons whilst, in alkaline solutions, olivine dissolution rates are pH-independent. The transition from one mode to the other is for pH values around 6 at 25 °C (Crundwell, 2014). These studies also stressed the inhibiting effects of the fluid silica activity and carbonate contents on olivine dissolution and the importance of the chemical processes occurring at the mineral surface (adsorption and desorption, protonation) during dissolution. They showed that the precipitation of secondary hydrous phases, carbonates and oxides and their kinetics were controlled by the thermodynamic and chemical parameters (e.g., P, T, pH, ionic strength, speciation as summarized by saturation indexes) whilst investigating the role of nucleation and surface processes. For instance, fast or slow precipitation kinetics determine whether a mineral thermodynamically stable according to activity diagrams and saturation indexes can be present or not (e.g., Bénézeth et al., 2011) and the formation of hydrated surface precursor complexes will facilitate the formation of hydrous species such as brucite (e.g., Pokrovsky and Schott, 2004). Most of studies on the kinetics of mineral dissolution and precipitation were realized at temperatures below 100 °C, nevertheless the rate-controlling mechanisms of these reactions are well understood (Pokrovsky and Schott, 2000a, 2000b; review in Crundwell, 2014 and Ruiz-Agudo et al., 2014)

and we posit that the conceptual models based on these studies could be used as a starting point to interpret the results of our four reactive percolation experiments.

We postulate first that the possible intermediate reaction paths for olivine serpentinization are controlled by the coupling between olivine dissolution, assumed to be dominantly controlled by proton activity at the fluid-mineral interface, and serpentine precipitation, which buffers the fluid composition (including pH, see Fig. 10). Flow and transport processes determine the *reaction domains* in which these interactions occur. As illustrated in Fig. 12, two end-member scenarios are proposed to summarize the interplay between these mechanisms. They are governed by the development of diffusive boundary layers at the fluid / mineral interface and by chemical gradients within these diffusive layers. As mentioned earlier, the thickness of diffusive layers is inversely proportional to the local value of Pe and, consequently, chemical gradients are directly correlated to local fluid velocity.

The first scenario, hereafter referred to as a *transport-controlled scenario* (Fig. 12a), characterizes low fluid velocity domains, where diffusive layers can grow and occupy significant pore volume. These diffusion-dominated "reaction domains" represent zones where mixing can occur and which are therefore favorable to chemical reactions (e.g., Luquot and Gouze, 2009). In these domains, fluid compositions will be controlled by that of dissolved olivine at the mineral surface and progressively equilibrate with the composition imposed by advecting fluids at the outer boundary of the diffusive domain. Chemical and charge gradients across the diffusive domain drive ionic (cation, anions) and proton exchanges respectively between the olivine surface and advecting fluids. Protons adsorption at the mineral surface induces the dissolution of olivine and the detachment of SiO_4^{4-} and Mg^{2+}. $MgOH^+(aq)$ is formed by the hydration of Mg^{2+} and adds up $MgOH^+(aq)$ of incoming fluids. Hydration of SiO_4^{4-} increases pH, which favors the precipitation of brucite after $MgOH^+(aq)$ in the diffusion-dominated "reaction domain". The early enrichments in SiO_2 $_{(aq)}$ and pH increase of the outlet fluids, which represent the advecting fluids in this model, implies that serpentine precipitation rates are slow compared to brucite precipitation rates as well as to the rate of proton and silica exchanges between the diffusion-dominated "reaction domain" and advecting fluids. As reaction progresses, a steady state will be reached: pH will stabilize and/or decrease slightly (Figs. 7, 10) as a result of the formation of brucite which, in turn, will favor serpentine formation, eventually after brucite (Reaction R3; Godard et al., 2013; Tutolo et al., 2018). The second end-member scenario, here referred to as the *kinetics-controlled scenario* (Fig. 12b), is associated to high fluid velocity zones, where the fast renewal of fluid at the mineral surface limits the development of the diffusive layer. The "reaction domain" then covers the full porous network and the mineral/fluid interface is namely undistinguishable from the outer diffusive layer boundary. In this advection-dominated "reaction domain", spreading will favor efficient transport of protons and chemical species while limiting their interactions in fluids and thus hinder chemical reactions. The sharp chemical gradient between olivine surface and advecting fluids favors high olivine dissolution kinetics and efficient detachment of SiO_4^{4-} and Mg^{2+}. The progressive increase in pH (Fig. 7) indicates that rates of olivine dissolution and hydration of SiO_4^{4-} are faster than the transport of hydrated species, $SiO_{2(aq)}$ and $MgOH^+(aq)$, out of the reactive zone. The belated stabilization of pH and evidence of silica trapping in fluid time series suggest a transient stage for the formation of serpentine, during which a silica rich layer could form at the fluid-mineral interface (e.g., Andreani et al., 2009; Daval et al., 2011; Pokrovsky and Schott, 2000a) until conditions favorable for serpentine precipitation are reached in the porous network. After 300 h, saturation relative to serpentine is achieved, serpentine (Spt) precipitates and consumes silica in excess. The serpentinization reaction then controls the mineral assemblage and the fluid composition following reaction path (R3).

These two end-members scenarios are not mutually exclusive at the scale of the studied samples: both diffusion and advection are effective
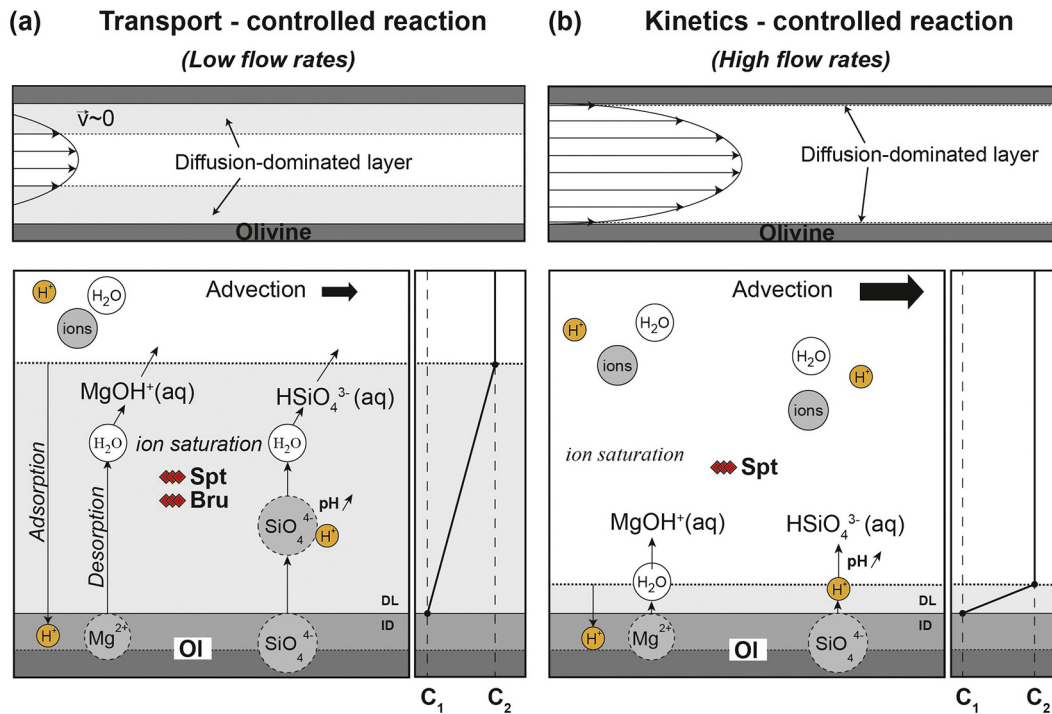
Fig. 12. End-members scenarios for incipient serpentinization at (a) low and (b) high flow rates. The distribution of the fluid velocity (v) in pores and flow paths determines the development of a diffusive boundary layer (DL) where $v \rightarrow 0$ at the mineral/fluid interface. The DL is large at low Q and is minimal for high Q (a-b). The surface of the olivine (Ol) is constituted of an ion detachment layer (ID) where fluid-rock reactions occur. The fluid is composed of water molecules (H_2O) (white circles), ions (grey circles) and protons (H^+) (yellow circles). The composition of the fluid at the outer boundary of the diffusive layer is that of the advected flow (C_2). When different from C_1, the composition of fluid in equilibrium with olivine, this difference in composition creates a chemical and electrical potential gradient in DL. The thickness of DL determines whether chemical and potential gradients will be low or high, which in turn will determine the mechanisms taking place in this layer (a) Transport controlled reaction paths are associated to low fluid velocity zones, which favors the development of diffusive layers and low chemical gradients between the olivine surface and advecting fluids. Proton transport toward the olivine surface is driven by the differences in electric charges between the dissolving olivine surface and advecting fluids. Protons adsorption at the mineral surface induces the stoichiometric dissolution of olivine, the detachment of SiO_4^{4-} and Mg^{2+} and the formation of $HSiO_4^{3-}$(aq) and $MgOH^+$(aq) respectively. The generation of $HSiO_4^{3-}$(aq) increases pH locally. The generation of $MgOH^+$(aq) coupled to the pH increase favors the saturation of brucite (Bru) and its precipitation together with serpentine (Spt) in the diffuse layer. (b) Kinetics controlled reaction are associated to high fluid velocity zones. The fast renewal of fluid at the mineral surface limits the thickness of the diffusive layer and produces sharp chemical gradients. Spreading limits the effects of fluid rock reactions at the mineral interface and favors the transport of $HSiO_4^{3-}$(aq) and $MgOH^+$(aq) out of the reactive zone. Serpentine (Spt) precipitates when super-saturation is reached in fluids flowing through the porous network.

mechanisms even if the macroscopic value of Pe is different from one experiment to the other.

The chemical mechanisms driving serpentinization reactions in the two end-member scenarios proposed here are similar to the scenarios proposed by Crundwell (2014); Lafay et al. (2012); Godard et al. (2013); Tutolo et al. (2018) for olivine dissolution and serpentinization in alkaline fluids and for serpentinization after brucite for the former (transport-controlled scenario), and to that proposed by Crundwell (2014); Seyfried and Dibble (1980); Allen and Seyfried (2003) for olivine dissolution in acidic fluids and serpentinization after Si-rich fluids for the latter (kinetics-controlled scenario). Transport controls local chemical fluxes and therefore the fluid compositions at the scale of the "reaction domain". In other words, these models suggest that local fluid composition is the main parameter governing reaction paths during our experiments. It noteworthy that pH in inlet and outlet fluids is slightly alkaline for all the experiments, suggesting that the transition from "alkaline" to "acidic" reaction paths occur most likely for pH(170 °C) around 6, that is within the alkaline domain for our experiments (neutral pH(170 °C) = 5.6). Interestingly, it is the same pH value as that suggested by Crundwell (2014) for reactions at 25 °C, suggesting that proton activity only (independently from temperature) would govern the change of kinetics for olivine dissolution.

Whatever the reaction paths, all experiments are characterized by a continuous decrease in Si compared to Mg (Figs. 8 and 10) and thus a continuous decrease in Si/Mg ratio (Appendix H Fig.H1). This variation could point to a decrease in the reactive surface areas over time. This process will produce a diminution of reaction rates that will ultimately end the reactions. This implies that the creation of new reactive surface area, via mechanisms such as fracturing (e.g., Kelemen and Hirth, 2012), is required to sustain these reactions over time.
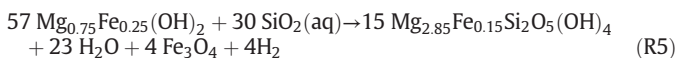
4.3. New insights on serpentinization of oceanic mantle lithosphere

Serpentinization of the oceanic mantle is generally pictured as a single step reaction of hydration of mantle minerals, producing serpentine, magnetite, hydrogen, and minor brucite (e.g., Reaction R1) and/or silica rich fluids, when the alteration of mantle pyroxene is also taken into account (e.g., Beard et al., 2009; Klein et al., 2013; McCollom and Bach, 2009). However, petrological and magnetic studies of serpentinized oceanic mantle basement (e.g., Bach et al., 2006; Oufi et al., 2002) and fluid measurements at ultramafic hosted vents (e.g., Donval et al., 1997; Kelley et al., 2001; Schmidt et al., 2011; Seyfried et al., 2015; Seyfried et al., 2011) provide evidence that serpentinization is a multistage process along mid-ocean ridges. Furthermore, detailed geochemical studies of the fluid time series sampled at ultramafic hosted vents along slow spread ridges show that these fluids sample a single source and therefore the measured variations in fluid compositions are ascribed to the development of different serpentinization reaction paths in the mantle basement (e.g., Bach et al., 2004; Bach et al., 2006; McCollom and Bach, 2009; Seyfried et al., 2015; Syverson et al., 2017; Tutolo et al., 2018). The mantle lithosphere exposed along slow spread oceanic centers is highly heterogeneous with intrusions of large gabbroic bodies (e.g., Cannat et al., 1997; Früh-Green et al., 2003) and/or locally overlain by thin basaltic crust (e.g., Cannat et al., 2006; Escartin

et al., 2017). The variability of observed serpentinization reaction paths is thus commonly ascribed to changes in the composition of serpentinizing hydrothermal fluids resulting from interactions with these different lithologies along flow paths (e.g., Andreani et al., 2014; Bach et al., 2004). Our experiments suggest that some of these observed chemical variations might be intrinsic to incipient serpentinization of olivine-rich rocks infiltrated by Mg-bearing seawater derived hydrothermal fluids, thus providing new insights on several questions critical to understand serpentinization processes in the sub-seafloor ultramafic basement.

4.3.1. Origin and fate of silica rich fluids during sub-seafloor serpentinization

Olivine hydration reactions predict the formation of brucite together with that of serpentine, yet brucite remains a minor component in serpentinized oceanic peridotites, observed dominantly in the least serpentinized peridotites (e.g., Bach et al., 2004). Based on petrological observations and compositional considerations, it was proposed that oceanic serpentinization occurred as a two-step reaction sequence with first the formation of Fe-bearing serpentine and brucite after olivine followed by a reaction of silicification of brucite (e.g. Bach et al., 2006) written as (assuming brucite does contain Fe):

$$57\,Mg_{0.75}Fe_{0.25}(OH)_2 + 30\,SiO_2(aq) \rightarrow 15\,Mg_{2.85}Fe_{0.15}Si_2O_5(OH)_4$$
$$+ 23\,H_2O + 4\,Fe_3O_4 + 4H_2 \qquad (R5)$$

The source of aqueous silica driving brucite silicification in the sub-seafloor mantle basement is inferred to be the alteration of the peridotite-forming pyroxenes (e.g., Bach et al., 2006; Beard et al., 2009; Frost et al., 2013), and of the pyroxene and plagioclase from neighbouring gabbroic intrusions (e.g., Bach et al., 2004; Boschi et al., 2006, 2008; Seyfried et al., 2015). Batch serpentinization experiments support this hypothesis as brucite is systematically lacking when pyroxene-bearing peridotites are altered (e.g., Klein et al., 2015) whilst it is often observed when olivine is altered (e.g., Malvoisin and Brunet, 2014).Yet, paradoxically, brucite is not described as being part of the secondary mineral assemblages produced after olivine hydration when Mg-rich fluids are used (e.g., Janecky and Seyfried, 1986; Seyfried et al., 2007; Seyfried and Dibble, 1980) except for the synthetic fluid inclusions experiments of Lamadrid et al. (2017). Another puzzling observation is the selective increase in silica activity in the early stages of batch serpentinization experiments using Mg-rich fluids (e.g., Klein et al., 2015; Seyfried et al., 2007). Reactive percolation experiments simulating interactions between olivine and Mg-rich seawater derived hydrothermal fluids show similar trends when injection flow rates are low ($Pe < 1$) (Godard et al., 2013 and this study). Similar to batch studies, reactive percolation outlet fluids record strong increases in silica activity, up to three times the composition of inlet fluids in our experiment. These ranges of variation are too similar to silica enrichments relative to seawater observed in the ultramafic-hosted hydrothermal vents (e.g., Lost City Hydrothermal Vent fluids (Seyfried et al., 2015)). Our results indicate that fast Mg-trapping and early yet transient brucite formation can be an efficient mechanism for increasing silica activity in hydrothermal fluids during incipient serpentinization. The development of these compositional trends is limited to diffusion dominated domains infiltrated by Mg-rich fluids nevertheless these conditions are analogous to low porosity mantle peridotites being infiltrated by seawater-derived fluids. These processes are however most likely short-lived in natural systems similar to what observed in batch experiments: the local increase in silica activity and the stabilization or decrease of pH produced by brucite precipitation will in turn favor serpentine precipitation as well as the extensive consumption of brucite. Minor brucite observed in poorly serpentinized peridotites is most likely preserved because of the slow kinetics of brucite silicification reactions (Tutolo et al., 2018) or incomplete reactions due to low fluid renewal (see below). Also, as serpentinization reactions progress,

Mg-activity should decrease in hydrothermal fluids in diffusion-dominated systems and serpentinization reaction paths tend toward those predicted assuming influx of pure water (e.g., R1) provided that minimal permeability is maintained.

Along oceanic spreading centres, high flow zones are often characterized by silica-rich lithologies, which are attributed to interaction with fluids having high silica activity (e.g., Bonnemains et al., 2017; Escartin et al., 2017; Karson et al., 2006; Paulick et al., 2006). Our results show that serpentinization reaction paths in advection-dominated domains favors leaching of Mg and precipitation of silica rich phases. The silica-rich phase is serpentine in our experiments but these results suggest a possible contribution of serpentinization reactions in enhancing silica trapping reactions along in the most permeable zones in the serpentinizing mantle (fractures, fault zones) at mid-ocean ridges.

4.3.2. Changes of volume for transport-controlled and kinetics-controlled reaction paths

The oceanic mantle lithosphere exposed along slow spreading ridges is commonly envisioned a multi-permeable media: oceanic detachment faults and fractures are the highly permeable zones allowing seawater derived fluids to penetrate deeply into the cooling mantle lithosphere (e.g., de Martin et al., 2007; Emmanuel and Berkowitz, 2006; Farough et al., 2016; Lowell, 2013; McCaig et al., 2007) while, at a smaller scale (cm- and below), the development of veins (e.g., Andreani et al., 2007), mesh networks and microcracks (e.g., Rouméjon et al., 2015) reveals the pervasive infiltration of fluids into the peridotite basement through an interplay between regional stress, thermal cracking and dissolution-precipitation reactions (e.g., Boudier et al., 2005; Plümper et al., 2012). Both advection and diffusion are expected to drive solute transport in the low permeability serpentinizing peridotites, with advection being most likely predominant in the mesh structure and veins, whilst diffusion should prevail along mineral boundaries and microcracks (Malvoisin and Brunet, 2014).

The two end member reaction paths shown by reactive-percolation experiments are expected to yield different local changes in the structure and permeability of the serpentinizing mantle rocks, through the precipitation of low density serpentine $+/-$ brucite at the expense of olivine (Table F.1, Appendix F). Transport controlled reaction paths will produce a lesser volume increase in diffusion-dominated domains (30% according to reaction R2) than kinetics controlled reaction paths in advection-dominated domains (42% according to reaction R3); however both predict lesser volume variations than the commonly used serpentinization relationship (43%- reaction R1). As a result, advection-dominated domains will be clogged more efficiently than diffusion-dominated domains even though olivine dissolution is more efficient (see text for Fig. 12 model). It is worth noting that the accumulation of stress due to fast precipitation localized in narrow zones such as olivine dissolution etch pits is considered as a possible mechanism for cracking and maintaining permeability in serpentinites (dissolution driven cracking; Plümper et al., 2012; Røyne and Jamtveit, 2015). The coupling of kinetics controlled serpentinization reaction paths and dissolution driven cracking could provide an efficient mechanism favoring continuous and pervasive flux of fluids from fault zones into the mantle peridotite basement. In contrast, in diffusion dominated domains, fluid renewal will most likely be controlled by permeability changes resulting from brucite and serpentine precipitation. These processes should in turn, reduce serpentinization reactions thus providing a mechanism for preservation of relict primary minerals often observed in abyssal peridotites (e.g., Hellebrand et al., 2002; Bach et al., 2004; Godard et al., 2008; D'errico et al., 2016).

5. Summary and conclusions

Serpentinization of ultramafic rocks at ridges occurs upon cooling of the oceanic lithosphere if seawater is available. To study the effect of solute transport during incipient stages of serpentinization, four reactive-percolation experiments were performed at different constant flow

rates. The experiments consisted in injecting artificial seawater into compressed San Carlos olivine powders at 170 °C and 25 MPa.

Proto-serpentine was formed in the four experiments but different trends were observed for low and high flow rates. Low flow rate experiments showed the precipitation of nodular aggregates on the reacted surface, a strong increase of silica concentration of the outlet fluid relative to magnesium and a slightly decrease of pH. Conversely, high flow rate experiments emphasized the precipitation of fibrous filaments, a strong increase of the magnesium concentration of the outlet fluid compared to silica and a slight increase of pH.

Flow and transport processes, here covering a range of 0.02 to 4 in term of Peclet number, appears to determine the length and time scale of the reaction domains where fluid-rock interactions takes place. Diffusive boundary layers, whose thickness is inversely proportional to local fluid velocities, develop at the fluid/mineral interface and control by chemical gradients in the vicinity of the reactive surfaces. Porous media contain zones of low fluid velocity where the diffusive layers can occupy a significant fraction of the pore volume and zones of fast velocities with reduced diffusive layer. For a given pore structure, the fraction of diffusion-controlled zones increases as the sample scale flow rate decreases. Accordingly, two end-member scenarios are proposed to describe incipient serpentinization reaction paths during reactive percolation experiments. These two scenarios depend on the efficiency of diffusion-controlled renewing of solutes at the mineral reactive surface:

1) Transport-controlled scenario occurs at low flow rate. In this case, the large amount of diffusion zones controls the exchanges between the mineral and the bulk fluid and furthermore allows efficient mixing of the reactants and products. The dissolution of olivine produces hydration of SiO_4^{4-} which increases pH and favors the precipitation of brucite after the Mg detached from olivine and the $MgOH^+$(aq) of incoming fluids. Eventually, serpentine will precipitate at the expense of brucite. This process could explain, in part, the absence of brucite in most oceanic hydrothermal systems.

2) Kinetics-controlled scenario occurs at high flow rates: the renewing of the reactants and products at the reaction surface is efficiently produced by advection. The sharp chemical gradients between the olivine surface and the bulk fluid trigger high olivine dissolution rate. However, the evidences of silica trapping and magnesium released suggest a transient stage for the formation of serpentine during which a silica rich layer could form at the fluid-mineral interface until conditions favorable for serpentine precipitation are reached in the porous network.

The development of compositional trends (e.g. Si-rich fluids or Mg-rich fluids) is strongly dependent on local flow rates at the scale of the fluid-mineral interface. The two scenarios described in this study can be related to processes occurring in ultramafic hosted hydrothermal systems along mid-ocean ridges: 1) the diffusion-dominated scenario is analogous to low porosity confined zones (i.e. along mineral boundaries and microcracks) where seawater-derived fluids infiltrate mantle peridotites. The local increase of pH resulting from olivine dissolution and the slow renewal of fluid in the pore leads to ion saturation and precipitation of brucite, then serpentine. 2) Advection-dominated scenario is analogous to highly permeable zones (i.e. oceanic detachment faults and fractures). High amounts of serpentine precipitate in this zone, which in turn clog flow paths more efficiently than diffusion-dominated domains.

Both these serpentinization reaction paths are observed in natural systems and commonly ascribed to changes in the composition of serpentinizing hydrothermal fluids resulting from interactions with different lithologies along flow paths. Our results suggest also a control of flow infiltration rate on the development of these different serpentinization reactions paths.

Acknowledgments

Appendix A-H. Supplementary data

Supplementary data to this article can be found online at https://doi.org/10.1016/j.lithos.2018.09.020.

References

Allen, D.E., Seyfried, W.E., 2003. Compositional controls on vent fluids from ultramafic-hosted hydrothermal systems at mid-ocean ridges: an experimental study at 400°C, 500 bars. Geochim. Cosmochim. Acta 67, 1531–1542. https://doi.org/10.1016/S0016-7037(02)01173-0.

Andreani, M., Daniel, I., 2013. Aluminium speeds up the hydrothermal alternation of olivine. Am. Mineral. 98, 1738–1744.

Andreani, M., Daniel, I., Pollet-Villard, M., 2013. Aluminium speeds up the hydrothermal alternation of olivine. Am. Mineral. 98, 1738–1744.

Andreani, M., Mével, C., Boullier, A.M., Escartín, J., 2007. Dynamic control on serpentine crystallization in veins: Constraints on hydration processes in oceanic peridotites. Geochem. Geophys. Geosyst. 8. https://doi.org/10.1029/2006GC001373.

Andreani, M., Luquot, L., Gouze, P., Godard, M., Gibert, B., 2009. Experimental study of carbon sequestration reactions controlled by the percolation of CO_2-rich brine through peridotites. Environ. Sci. Technol. 43, 1226–1231.

Andreani, M., Escartin, J., Delacour, A., Ildefonse, B., Godard, M., Dyment, J., Fallick, A., Fouquet, Y., 2014. Tectonic structure, lithology, and hydrothermal signature of the Rainbow massif (Mid-Atlantic Ridge 36°14'N). Geochem. Geophys. Geosyst. 18, 1541–1576. https://doi.org/10.1002/2014GC005684.

Bach, W., Garrido, C.J., Paulick, H., Harvey, J., Rosner, M., 2004. Seawater-peridotite interactions: first insights from ODP Leg 209, MAR 15°N. Geochem. Geophys. Geosyst. 5. https://doi.org/10.1029/2004GC000744.

Bach, W., Paulick, H., Garrido, C.J., Ildefonse, B., Meurer, W.P., Humphris, S.E., 2006. Unraveling the Sequence of Serpentinization Reactions: Petrography, Mineral Chemistry, and Petrophysics of Serpentinites From MAR 15°N (ODP Leg 209 , Site 1274). 33, pp. 4–7. https://doi.org/10.1029/2006GL025681.

Bandura, A.V., Lvov, S.N., 2006. The Ionization constant of water over wide ranges of temperature and density. J. Phys. Chem. Ref. Data 35, 15–30. https://doi.org/10.1063/1.1928231.

Beard, J.S., Frost, B.R., Fryer, P., McCaig, A., Searle, R., Ildefonse, B., Zinin, P., Sharma, S.K., 2009. Onset and progression of serpentinization and magnetite formation in Olivine-rich troctolite from IODP hole U1309D. J. Petrol. 50, 387–403. https://doi.org/10.1093/petrology/egp004.

Bénézeth, P., Saldi, G.D., Dandurand, J.L., Schott, J., 2011. Experimental determination of the solubility product of magnesite at 50 to 200°C. Chem. Geol. 286, 21–31. https://doi.org/10.1016/j.chemgeo.2011.04.016.

Berndt, M.E., Allen, D.E., Seyfried, W.E., 1996. Reduction of CO_2 during serpentinization of olivine at 300°C and 500 bar. Geology 24, 351–354. https://doi.org/10.1130/0091-7613(1996)024<0351.

Bethke, C.M., 1996. Geochemical Reaction Modeling. Oxford University Press, New York 397 p.

Bischoff, J.L., Seyfried, W.E., 1978. Hydrothermal Chemistry of seawater from 25° to 350°C. Am. J. Sci. 278, 838–860.

Bodinier, J., Godard, M., 2003. Orogenic, ophiolitic, and abyssal peridotites. Treatise on Geochemistry. Elsevier, pp. 1–73 https://doi.org/10.1016/B0-08-043751-6/02004-1.

Bonnemains, D., Escartin, J., Mevel, M., Andreani, M., Verlaguet, A., 2017. Pervasive silicification and hanging wall overplating along the 13°20'N oceanic detachment fault (Mid-Atlantic Ridge). Geochem. Geophys. Geosyst., 1–26 https://doi.org/10.1002/2016GC006679.

Boschi, C., Früh-Green, G.L., Delacour, A., Karson, J.A., Kelley, D.S., 2006. Mass transfer and fluid flow during detachment faulting and development of an oceanic core complex, Atlantis Massif (MAR 30°N). Geochem. Geophys. Geosyst. 7. https://doi.org/10.1029/2005GC001074.

Boschi, C., Dini, A., Früh-Green, G.L., Kelley, D.S., 2008. Isotopic and element exchange during serpentinization and metasomatism at the Atlantis Massif (MAR 30°N): Insights from B and Sr isotope data. Geochim. Cosmochim. Acta 72, 1801–1823. https://doi.org/10.1016/j.gca.2008.01.013.

Boudier, F., Nicolas, A., Mainprice, D., 2005. Does anisotropy of thermal contraction control hydrothermal circulation at the moho level below fast spreading oceanic ridges? Int. Geol. Rev. 47, 101–112. https://doi.org/10.2747/0020-6814.47.1.101.

Cannat, M., Lagabrielle, Y., Bougault, H., Casey, J.F., de Coutures, N., Dmitriev, L., Fouquet, Y., 1997. Ultramafic and gabbroic exposures at the Mid-Atlantic Ridge: geological mapping in the 15°N region. Tectonophysics 279, 193–213.

Cannat, M., Sauter, D., Mendel, V., Ruellan, E., Okino, K., Escartin, J., Combier, V., Baala, M., 2006. Modes of seafloor generation at a melt-poor ultraslow-spreading ridge. Geology 34, 605–608. https://doi.org/10.1130/G22486.1.

Charlou, J.L., Donval, J.P., Konn, C, Ondréas, H., Fouquet, Y., Jean-Baptiste, P., Fourré, E., 2013. High production and fluxes of H2 and CH4 and evidence of abiotic hydrocarbon synthesis by serpentinization in ultramafic-hosted hydrothermal systems on the mid-Atlantic ridge. Divers. Hydrothermal Syst. Slow Spreading Ocean Ridges, 265–296 https://doi.org/10.1029/2008GM000732.

Chen, Y., Brantley, S.L., 2000. Dissolution of forsteritic olivine at 65°C and 2 < pH < 5. Chem. Geol. 165, 267–281. https://doi.org/10.1016/S0009-2541(99)00177-1.

Crundwell, F.K., 2014. The mechanism of dissolution of minerals in acidic and alkaline solutions: Part II Application of a new theory to silicates, aluminosilicates and quartz. Hydrometallurgy 149, 265–275. https://doi.org/10.1016/j.hydromet.2014.07.003.

Daval, D., Sissmann, O., Menguy, N., Saldi, G.D., Guyot, F., Martinez, I., Corvisier, J., Garcia, B., Machouk, I., Knauss, K.G., Hellmann, R., 2011. Influence of amorphous silica layer formation on the dissolution rate of olivine at 90°C and elevated pCO2. Chem. Geol. 284, 193–209. https://doi.org/10.1016/j.chemgeo.2011.02.021.

Donval, J.P., Charlou, J.L., Douville, E., Knoery, J., Fouquet, Y., Ponzevera, E., Jean-Baptiste, P., Stievenard, M., German, C., 1997. High H2 and CH4 content in hydrothermal fluids from rainbow site newly sampled at 36°14' on the AMAR segment, Mid-Atlantic Ridge (diving Flores cruise, July 1997). Comparison with other sites. EOS Trans. Am. Geophys. Union 78, 832.

Douville, E., Charlou, J.L., Oelkers, E.H., Bienvenu, P., Jove Colon, C.F., Donval, J.P., Fouquet, Y., Prieur, D., Appriou, P., 2002. The rainbow vent fluids (36°14'N, MAR): the influence of ultramafic rocks and phase separation on trace metal content in Mid-Atlantic Ridge hydrothermal fluids. Chem. Geol. 184, 37–48. https://doi.org/10.1016/S0009-2541(01)00351-5.

Emmanuel, S., Berkowitz, B., 2006. Suppression and stimulation of seafloor hydrothermal convection by exothermic mineral hydration. Earth Planet. Sci. Lett. 243, 657–668. https://doi.org/10.1016/j.epsl.2006.01.028.

Escartín, J., Hirth, G., Evans, B., 2001. Strength of slightly serpentinized peridotites: Implications for the tectonics of oceanic lithosphere. Geology 29, 1023–1026. https://doi.org/10.1130/0091-7613(2001)029<1023:SOSSPI>2.0.CO.

Evans, B.W., 2004. The serpentinite multisystem revisited : Chrysotile is metastable. Int. Geol. Rev. 46, 479–506.

Evans, B.W., 2008. Control of the products of serpentinization by the Fe2+Mg−1 exchange potential of olivine and orthopyroxene. J. Petrol. 49, 1873–1887. https://doi.org/10.1093/petrology/egn050.

Evans, B.W., Hattori, K., Baronnet, A., 2013. Serpentinite: what, why, where? Elements 9, 99–106. https://doi.org/10.2113/gselements.9.2.99.

Farough, A., Moore, D.E., Lockner, D.A., Lowell, R.P., 2016. Evolution of fracture permeability of ultramafic rocks undergoing serpentinization at hydrothermal conditions: an experimental study. Geochem. Geophys. Geosyst. 17, 44–55. https://doi.org/10.1002/2015GC005973.

Földvári, M., 2011. Handbook of Thermogravimetric System of Minerals and its Use in Geological Practice (Geological Institute of Hungary).

Frost, B.R., Evans, K.A., Swapp, S.M., Beard, J.S., Mothersole, F.E., 2013. The process of serpentinization in dunite from New Caledonia. Lithos 178, 24–39. https://doi.org/10.1016/j.lithos.2013.02.002.

Früh-Green, G.L., Kelley, D.S., Bernasconi, S.M., Karson, J.A., Ludwig, K.A., Butterfield, D.A., Boschi, C., Proskurowski, G., 2003. 30,000 Years of Hydrothermal Vent Field. Science 301, 495–498 (80-.).

Früh-Green, G.L., Connolly, J.A.D., Plas, A., Kelley, D.S., Grobéty, B., 2004. Serpentinization of oceanic peridotites: Implications for geochemical cycles and biological activity. Geophys. Monogr. Ser. 144, 119–136. https://doi.org/10.1029/144GM08.

Gerdemann, S.J., O'Connor, W.K., Dahlin, D.C., Penner, L.R., Rush, H., 2007. Ex situ aqueous mineral carbonation. Environ. Sci. Technol. 41, 2587–2593. https://doi.org/10.1021/es0619253.

Giammar, D.E., Bruant, R.G., Peters, C.A., 2005. Forsterite dissolution and magnesite precipitation at conditions relevant for deep saline aquifer storage and sequestration of carbon dioxide. Chem. Geol. 217, 257–276. https://doi.org/10.1016/j.chemgeo.2004.12.013.

Gislason, S.R., Oelkers, E.H., 2003. Mechanism, rates, and consequences of basaltic glass dissolution: II. An experimental study of the dissolution rates of basaltic glass as a function of pH and temperature. Geochim. Cosmochim. Acta 67, 3817–3832. https://doi.org/10.1016/S0016-7037(03)00176-5.

Gjetvaj, F., Russian, A., Gouze, P., Dentz, M., 2015. Dual control of flow field heterogeneity and immobile porosity on non-Fickian transport in Berea sandstone. Water Resour. Res. 51, 8273–8293. https://doi.org/10.1002/ 2015WR017645.

Godard, M., Lagabrielle, Y., Alard, O., Harvey, J., 2008. Geochemistry of the highly depleted peridotites drilled at ODP Sites 1272 and 1274 (Fifteen-twenty Fracture Zone, Mid-Atlantic Ridge): Implications for mantle dynamics beneath a slow spreading ridge. Earth Planet. Sci. Lett. 267, 410–425. https://doi.org/10.1016/j.epsl.2007.11.058.

Godard, M., Luquot, L., Andreani, M., Gouze, P., 2013. Incipient hydration of mantle lithosphere at ridges: a reactive-percolation experiment. Earth Planet. Sci. Lett. 371–372, 92–102. https://doi.org/10.1016/j.epsl.2013.03.052.

Gouze, P., Luquot, L., 2011. X-ray microtomography characterization of porosity, permeability and reactive surface changes during dissolution. J. Contam. Hydrol. 120–121, 44–55. https://doi.org/10.1016/j.jconhyd.2010.07.004.

Hänchen, M., Prigiobbe, V., Storti, G., Seward, T.M., Mazzotti, M., 2006. Dissolution kinetics of fosteritic olivine at 90-150 °C including effects of the presence of CO2.

Geochim. Cosmochim. Acta 70, 4403–4416. https://doi.org/10.1016/j.gca.2006.06.1560.

Hatakeyama, K., Katayama, I., Hirauchi, K., Michibayashi, K., 2017. Mantle hydration along outer-rise faults inferred from serpentinite permeability. Sci. Rep. 7, 13870. https://doi.org/10.1038/s41598-017-14309-9.

Helgeson, H.C., Delany, J.M., Nesbitt, H.W., Bird, D.K., 1978. Summary and critique of the thermodynamic properties of rock-forming minerals. Am. J. Sci. 278-A, 229.

Helgeson, H.C., Kirkham, D.H., Flowers, G.C., 1981. Theoretical prediction of the thermodynamic behavior of aqueous electrolytes at high pressures and temperatures. Calculation of activity coefficients, osmotic coefficients, and apparent molal and standard and relative partial molal properties to 600°C and 5 kbar. Am. J. Sci. 281, 1249–1516.

Hellebrand, E., Snow, J., Hoppe, P., Hofmann, A., 2002. Garnet-field melting and late-stage refertilization in "residual" abyssal peridotites from the Central Indian Ridge. J. Petrol. 43, 2305–2338.

Hirose, T., Hayman, N.W., 2008. Structure, permeability, and strength of a fault zone in the footwall of an oceanic core complex, the Central Dome of the Atlantis Massif, Mid-Atlantic Ridge, 30°N. J. Struct. Geol. 30, 1060–1071. https://doi.org/10.1016/j.jsg.2008.04.009.

Janecky, D.R., Seyfried, W.E., 1986. Hydrothermal Serpentinization of peridotite within the oceanic-Crust: Experimental investigations of mineralogy and major element chemistry. Geochim. Cosmochim. Acta 50, 1357–1378. https://doi.org/10.1016/0016-7037(86)90311-X.

Johnson, J.W., Oelkers, E.H., Helgeson, H.C., 1992. SUPCRT92: a software package for calculating the standard molal thermodynamic properties of minerals, gases, aqueous species, and reactions from 1 bar to 5000 bar and 0 to 1000°C. Comput. Geosci. 18, 899–947.

Karson, J.A., Früh-Green, G.L., Kelley, D.S., Williams, E.A., Yoerger, D.R., Jakuba, M., 2006. Detachment shear zone of the Atlantis Massif core complex, Mid-Atlantic Ridge, 30°N. Geochemistry, Geophys. Geosystems 7. https://doi.org/10.1029/2005GC001109.

Kelemen, P.B., Hirth, G., 2012. Reaction-driven cracking during retrograde metamorphism: Olivine hydration and carbonation. Earth Planet. Sci. Lett. 345–348, 81–89. https://doi.org/10.1016/j.epsl.2012.06.018.

Kelley, D.S., Karson, J.A., Blackman, D.K., Fruh-Green, G.L., Butterfield, D.A., Lilley, M.D., Olson, E.J., Schrenk, M.O., Roe, K.K., Lebon, G.T., Rivizzigno, P., 2001. An off-axis hydrothermal vent field near the Mid-Atlantic Ridge at 30° N. Nature 412, 145–149.

Kestin, J., Khalifa, E., Correira, R., 1981. Tables of the dynamic and kinematic viscosity of aqueous KCl Solutions in the temperature range 25–150°C and the pressure range 0.1-35 MPa. Data 10, 57–70.

Klein, F., Garrido, C.J., 2011. Thermodynamic constraints on mineral carbonation of serpentinized peridotite. Lithos 126, 147–160. https://doi.org/10.1016/j.lithos.2011.07.020.

Klein, F., Bach, W., McCollom, T.M., 2013. Compositional controls on hydrogen generation during serpentinization of ultramafic rocks. Lithos 178, 55–69. https://doi.org/10.1016/j.lithos.2013.03.008.

Klein, F., Grozeva, N.G., Seewald, J.S., McCollom, T.M., Humphris, S.E., Moskowitz, B., Berquo, T.S., Kahl, W.A., 2015. Fluids in the Crust. Experimental constraints on fluid-rock reactions during incipient serpentinization of harzburgite. Am. Mineral. 100, 991–1002. https://doi.org/10.2138/am-2015-5112.

Klein, F., McCollom, T., 2013. From serpentinization to carbonation: New insights from a CO2 injection experiment. EPSL 379, 137–145. https://doi.org/10.1016/j.epsl.2013.08.017.

Lafay, R., Montes-Hernandez, G., Janots, E., Chiriac, R., Findling, N., Toche, F., 2012. Mineral replacement rate of olivine by chrysotile and brucite under high alkaline conditions. J. Cryst. Growth 347, 62–72. https://doi.org/10.1016/j.jcrysgro.2012.02.040.

Lamadrid, H.M., Rimstidt, J.D., Schwarzenbach, E.M., Klein, F., Ulrich, S., Dolocan, A., Bodnar, R.J., 2017. Effect of water activity on rates of serpentinization of olivine. Nat. Commun. 8, 1–9. https://doi.org/10.1038/ncomms16107.

Lowell, R.P., 2013. Hydrothermal Circulation at Slow Spreading Ridges: Analysis of Heat sources and Heat transfer Processes. Divers. Hydrothermal Syst. Slow Spreading Ocean Ridges, 11–26 https://doi.org/10.1029/2008GM000758.

Lowell, R.P., Rona, P.A., 2002. Seafloor hydrothermal systems driven by the serpentinization of peridotite. Geophys. Res. Lett. 29, 0–3. https://doi.org/10.1029/2001GL014411.

Luhmann, A., Tutolo, B., Bagley, B., Mildner, D.F.R., Scheuermann, P.P., Feinberg, J.M., Ignatyev, K., Seyfried, W.E., 2017. Chemical and physical changes during seawater flow through intact dunite cores: an experimental study at 150–200°C. Geochim. Cosmochim. Acta 214, 86–114. https://doi.org/10.1016/j.gca.2017.07.020.

Luquot, L., Gouze, P., 2009. Experimental determination of porosity and permeability changes induced by injection of CO2 into carbonate rocks. Chem. Geol. 265, 148–159. https://doi.org/10.1016/j.chemgeo.2009.03.028.

MacDonald, A.H., Fyfe, W.S., 1985. Rate of serpentinization in seafloor environments. Tetonophysics 116, 123–135.

Maffione, M., Morris, A., Plümper, O., Van Hinsbergen, D., 2014. Magnetic properties of variably serpentinized peridotites and their implication for the evolution of oceanic core complexes. Geochem. Geophys. Geosyst. 15, 923–944. https://doi.org/10.1002/2013GC004993.

Malvoisin, B., Brunet, F., 2014. Water diffusion-transport in a synthetic dunite: Consequences for oceanic peridotite serpentinization. Earth Planet. Sci. Lett. 403, 263–272. https://doi.org/10.1016/j.epsl.2014.07.004.

Malvoisin, B., Brunet, F., Carlut, J., Rouméjon, S., Cannat, M., 2012. Serpentinization of oceanic peridotites: 2. Kinetics and processes of San Carlos olivine hydrothermal alteration. J. Geophys. Res. Solid Earth 117, 1–13. https://doi.org/10.1029/2011JB008842.

Marcaillou, C., Muñoz, M., Vidal, O., Parra, T., Harfouche, M., 2011. Mineralogical evidence for H$_2$ degassing during serpentinization at 300°C and 300bar. Earth Planet. Sci. Lett. 303, 281–290. https://doi.org/10.1016/j.epsl.2011.01.006.

Martin, B., Fyfe, W.S., 1970. Some experimental and theoretical observations on the kinetics of hydration reactions with particular reference to serpentinization. Chem. Geol. 6, 185–202.

de Martin, B.J., Reves-Sohn, R.A., Canales, J.P., Humphris, S.E., 2007. Kinematics and geometry of active detachment faulting beneath the Trans-Atlantic geotraverse (TAG) hydrothermal field on the Mid-Atlantic Ridge. Geology 35, 711–714. https://doi.org/10.1130/G23718A.1.

McCaig, A.M., Cliff, R.A., Escartin, J., Fallick, A.E., MacLeod, C.J., 2007. Oceanic detachment faults focus very large volumes of black smoker fluids. Geology 35, 935–938. https://doi.org/10.1130/G23657A.1.

McCollom, T.M., Bach, W., 2009. Thermodynamic constraints on hydrogen generation during serpentinization of ultramafic rocks. Geochim. Cosmochim. Acta 73, 856–875. https://doi.org/10.1016/j.gca.2008.10.032.

Mccollom, T.M., Klein, F., Robbins, M., Moskowitz, B., Jo, N., Berquo, T.S., Bach, W., Templeton, A., 2016. Temperature trends for reaction rates, hydrogen generation, and partitioning of iron during experimental serpentinization of olivine. Geochem. Cosmochim. Acta 181, 175–200. https://doi.org/10.1016/j.gca.2016.03.002.

Mével, C., 2003. Serpentinization of abyssal peridotites at mid-ocean ridges. Compt. Rendus Geosci. 335, 825–852. https://doi.org/10.1016/j.crte.2003.08.006.

Millero, F.J., Feistel, R., Wright, D.G., McDougall, T.J., 2008. The composition of standard seawater and the definition of the reference-composition salinity scale. Deep Sea Res. Part I Oceanogr. Res. Pap. 55, 50–72. https://doi.org/10.1016/j.dsr.2007.10.001.

Morse, J.W., Arvidson, R.S., 2002. The dissolution kinetics of major sedimentary carbonate minerals. Earth-Sci. Rev. 58, 51–84.

Noiriel, C., Madé, B., Gouze, P., 2007. Impact of coating development on the hydraulic and transport properties in argillaceous limestone fracture. Water Resour. Res. 43. https://doi.org/10.1029/2006WR005379.

O'Connor, W.K., Dahlin, D.C., Nilsen, D.N., Rush, G.E., Walters, R.P., Turner, P.C., 2001. Carbon dioxide sequestration by direct mineral carbonation: results from recent studies and current status. 1st Annu. DOE Carbon Sequestration Conf. Washington, D.C. 11.

O'Connor, W., Dahlin, D., Rush, G., Gerdemann, S., Penner, L.R., Nilsen, D., 2005. Aqueous Mineral Carbonation. National Energy Technology Laboratory, Albany Research Center, Office of Fossil Energy, US DOE.

Oelkers, E.H., 2001. An experimental study of forsterite dissolution rates as a function of temperature and aqueous Mg and Si concentrations. Chem. Geol. 175, 485–494. https://doi.org/10.1016/S0009-2541(00)00352-1.

Ogasawara, Y., Okamoto, A., Hirano, N., Tsuchiya, N., 2013. Coupled reactions and silica diffusion during serpentinization. Geochim. Cosmochim. Acta 119, 212–230. https://doi.org/10.1016/j.gca.2013.06.001.

O'Hanley, D.S., 1996. Serpentinites. Oxford University Press.

Okamoto, A., Ogasawara, Y., Ogawa, Y., Tsuchiya, N., 2011. Progress of hydration reactions in olivine-H$_2$O and orthopyroxenite-H$_2$O systems at 250°C and vapor-saturated pressure. Chem. Geol. 289, 245–255. https://doi.org/10.1016/j.chemgeo.2011.08.007.

Oufi, O., Cannat, M., Horen, H., 2002. Magnetic properties of variably serpentinized abyssal peridotites. J. Geophys. Res. 107, 2095. https://doi.org/10.1029/2001JB000549.

Palandri, J.L., Reed, M.H., 2004. Geochemical models of metasomatism in ultramafic systems: Serpentinization, rodingitization, and seafloor carbonate chimney precipitation. Geochim. Cosmochim. Acta 68, 1115–1133. https://doi.org/10.1016/j.gca.2003.08.006.

Paulick, H., Bach, W., Godard, M., De Hoog, J.C.M., Suhr, G., Harvey, J., 2006. Geochemistry of abyssal peridotites (Mid-Atlantic Ridge, 15°20′N, ODP Leg 209): Implications for fluid/rock interaction in slow spreading environments. Chem. Geol. 234, 179–210. https://doi.org/10.1016/j.chemgeo.2006.04.011.

Pens, M., Andreani, M., Daniel, I., Perrillat, J.P., Cardon, H., 2016. Contrasted effect of aluminum on the serpentinization rate of olivine and orthopyroxene under hydrothermal conditions. Chem. Geol. 441, 256–264. https://doi.org/10.1016/j.chemgeo.2016.08.007.

Peuble, S., Andreani, M., Godard, M., Gouze, P., Barou, F., Van de Moortele, B., Mainprice, D., Reynard, B., 2015a. Carbonate mineralization in percolated olivine aggregates : linking effects of crystallographic orientation and fluid flow. Am. Mineral. 100, 474–482.

Peuble, S., Godard, M., Luquot, L., Andreani, M., Martinez, I., Gouze, P., 2015b. CO$_2$ geological storage in olivine rich basaltic aquifers: New insights from reactive-percolation experiments. Appl. Geochem. 52, 174–190. https://doi.org/10.1016/j.apgeochem.2014.11.024.

Philibert, J., 2005. One and a half Century of Diffusion: Fick, Einstein, before and beyond. Diffus. Fundam. 4, 1–19.

Plümper, O., Røyne, A., Magrasó, A., Jamtveit, B., 2012. The interface-scale mechanism of reaction-induced fracturing during serpentinization. Geology 40, 1103–1106. https://doi.org/10.1130/G33390.1.

Pokrovsky, O.S., Schott, J., 2000a. Kinetics and mechanism of forsterite dissolution at 25°C and pH from 1 to 12. Geochim. Cosmochim. Acta 64, 3313–3325. https://doi.org/10.1016/S0016-7037(00)00434-8.

Pokrovsky, O.S., Schott, J., 2000b. Forsterite surface composition in aqueous solutions: a combined potentiometric, electrokinetic, and spectroscopic approach. Geochim. Cosmochim. Acta 64, 3299–3312. https://doi.org/10.1016/S0016-7037(00)00435-X.

Pokrovsky, O.S., Schott, J., 2004. Experimental study of brucite dissolution and precipitation in aqueous solutions: Surface speciation and chemical affinity control. Geochim.Cosmochim. Acta 68, 31–45. https://doi.org/10.1016/S0016-7037(03)00238-2.

Prigiobbe, V., Costa, G., Baciocchi, R., Hänchen, M., Mazzotti, M., 2009. The effect of CO$_2$ and salinity on olivine dissolution kinetics at 120°C. Chem. Eng. Sci. 64, 3510–3515. https://doi.org/10.1016/j.ces.2009.04.035.

Rimstidt, J.D., Brantley, S.L., Olsen, A.A., 2012. Systematic review of forsterite dissolution rate data. Geochim. Cosmochim. Acta 99, 159–178. https://doi.org/10.1016/j.gca.2012.09.019.

Rosso, J.J., Rimstidt, D.J., 2000. A high resolution study of forsterite dissolution rates. Geochim. Cosmochim. Acta 64, 797–811. https://doi.org/10.1016/S0016-7037(99)00354-3.

Rouméjon, S., Cannat, M., Agrinier, P., Godard, M., Andreani, M., 2015. Serpentinization and Fluid pathways in tectonically exhumed peridotites from the southwest indian ridge (62–65°E). J. Petrol. 56, 703–734. https://doi.org/10.1093/petrology/egv014.

Røyne, A., Jamtveit, B., 2015. Pore-scale controls on reaction-driven fracturing. Rev. Mineral. Geochem. 80, 25–44. https://doi.org/10.2138/rmg.2015.80.02.

Rudge, J.F., Kelemen, P.B., Spiegelman, M., 2010. A simple model of reaction-induced cracking applied to serpentinization and carbonation of peridotite. Earth Planet. Sci. Lett. 291, 215–227. https://doi.org/10.1016/j.epsl.2010.01.016.

Ruiz-Agudo, E., Putnis, C.V., Putnis, A., 2014. Coupled dissolution and precipitation at mineral – fluid interfaces. Chem. Geol. 383, 132–146. https://doi.org/10.1016/j.chemgeo.2014.06.007.

Schmidt, K., Garbe-Schönberg, D., Koschinsky, A., Strauss, H., Jost, C.L., Klevenz, V., Königer, P., 2011. Fluid elemental and stable isotope composition of the Nibelungen hydrothermal field (8°18'S, Mid-Atlantic Ridge): Constraints on fluid-rock interaction in heterogeneous lithosphere. Chem. Geol. 280, 1–18. https://doi.org/10.1016/j.chemgeo.2010.07.008.

Schroeder, T., John, B., Frost, B.R., 2002. Geologic implications of seawater circulation through peridotite exposed at slow-spreading mid-ocean ridges. Geology 30, 367–370. https://doi.org/10.1130/0091-7613(2002)030<0367:GIOSCT>2.0.CO;2.

Seyfried, W.E., Dibble, W.E., 1980. Seawater-peridotite interaction at 300°C and 500 bars : implications for the origin of oceanic serpentinites. Geochim. Cosmochim. Acta 44, 309–321.

Seyfried, W.E., Foustoukos, D.I., Fu, Q., 2007. Redox evolution and mass transfer during serpentinization: an experimental and theoretical study at 200°C, 500 bar with implications for ultramafic-hosted hydrothermal systems at Mid-Ocean Ridges. Geochim. Cosmochim. Acta 71, 3872–3886. https://doi.org/10.1016/j.gca.2007.05.015.

Seyfried, W.E., Pester, N.J., Ding, K., Rough, M., 2011. Vent fluid chemistry of the Rainbow hydrothermal system (36°N, MAR): phase equilibria and in situ pH controls on subseafloor alteration processes. Geochim. Cosmochim. Acta 75, 1574–1593. https://doi.org/10.1016/j.gca.2011.01.001.

Seyfried, W.E., Pester, N., Fu, Q., 2013. Phase equilibria controls on the chemistry of vent fluids from hydrothermal systems on slow spreading ridges: reactivity of plagioclase and olivine solid solutions and the pH-silica connection. Divers. Hydrothermal Syst. Slow Spreading Ocean Ridges, 297–320 https://doi.org/10.1029/2009GM000854.

Seyfried, W.E., Pester, N.J., Tutolo, B.M., Ding, K., 2015. The lost City hydrothermal system: Constraints imposed by vent fluid chemistry and reaction path models on subseafloor heat and mass transfer processes. Geochim. Cosmochim. Acta 163, 59–79. https://doi.org/10.1016/j.gca.2015.04.040.

Shock, E.L., Helgeson, H.C., 1988. Calculation of the thermodynamic and transport properties of aqueous species at high pressures and temperatures: Correlation algorithms for ionic species and equation of state predictions to 5 kb and 1000°C. Geochim. Cosmochim. Acta 52, 2009–2036. https://doi.org/10.1016/0016-7037(88)90181-0.

Shock, E.L., Helgeson, H.C., Sverjensky, D.A., 1989. Calculation of the thermodynamic and transport properties of aqueous species at high pressures and temperatures: Standard partial molal properties of inorganic neutral species. Geochim. Cosmochim. Acta 53, 2157–2183. https://doi.org/10.1016/0016-7037(89)90341-4.

Shock, E.L., Sassani, D.C., Willis, M., Sverjensky, D.A., 1997. Inorganic species in geologic fluids: Correlations among standard molal thermodynamic properties of aqueous ions and hydroxide complexes. Geochim. Cosmochim. Acta 61, 907–950. https://doi.org/10.1016/S0016-7037(96)00339-0.

Siena, M., Hyman, J.D., Riva, M., Guadagnini, A., Winter, C.J., Smolarkiewic, P.K., Gouze, P., Sadhukhan, S., Inzoli, F., Guedon, G., Colombo, E., 2015. Direct numerical simulation of fully saturated flow in natural porous media at the pore scale: a comparison of three computational systems. Comput. Geosci. 19, 423–437. https://doi.org/10.1007/s10596-015-9486-7.

Stanger, G., Neal, C., 1994. The occurrence and chemistry of huntite from Oman. Chem. Geol. 112, 247–254. https://doi.org/10.1016/0009-2541(94)90027-2.

Steefel, C.I., Maher, K., 2009. Fluid-rock interaction: a reactive transport approach. Rev. Mineral. Geochem. 70, 485–532. https://doi.org/10.2138/rmg.2009.70.11.

Summerhayes, C.P., Thorpe, S.A., 1996. Oceanography: An Illustrated Guide. Manson Publishing Co. via Oxford University Press, Oxford.

Syverson, D.D., Tutolo, B.M., Borrok, D.M., Seyfried, W.E., 2017. Serpentinization of olivine at 300°C and 500 bars: an experimental study examining the role of silica on the reaction path and oxidation state of iron. Chem. Geol. 475, 122–134. https://doi.org/10.1016/j.chemgeo.2017.11.006.

Tutolo, B.M., Luhmann, A.J., Tosca, N.J., Seyfried, W.E., 2018. Serpentinization as a reactive transport process: the brucite silicification reaction. Earth Planet. Sci. Lett. 1, 1–13. https://doi.org/10.1016/j.epsl.2017.12.029.

Viti, C., 2010. Serpentine minerals discrimination by thermal analysis. Am. Mineral. 95, 631–638. https://doi.org/10.2138/am.2010.3366.

Wegner, W., Ernst, W., 1983. Experimentally determined hydration and dehydration reaction rates in the system MgO-SiO$_2$-H$_2$O. Am. J. Sci. 283–A, 151–180.

Wolery, T., Jarek, R.L., 2003. Software User's Manual EQ3/6, Version 8.0. Sandia National Laboratories, Albuquerque, New Mexico.

Zeebe, R.E., Wolf-Gladrow, D., 2001. CO$_2$ in Seawater: Equilibrium, Kinetics, Isotopes. Elsevier Oceanography series, New York.